Analysis of Metal-Organic Framework Stability, Antimicrobial Properties, and Dental Applications

Student PI:
Benjamin Marusko
Biology Major, Chemistry Minor
Florida Southern College
111 Lake Hollingsworth Dr.
Lakeland, FL, 33801
Phone: (937) 815-2431
E-mail: bmarusko0@gmail.com

Advisors:
Jarrod F. Eubank, Ph.D.
Associate Professor of Chemistry
Chemistry, Biochemistry and Physics Department
Florida Southern College
111 Lake Hollingsworth Dr.
Lakeland, FL, 33801
E-mail: jeubank@flsouthern.edu

Melanie Langford, Ph.D.
Associate Professor of Marine Biology
Biology Department
Florida Southern College
111 Lake Hollingsworth Dr.
Lakeland, FL, 33801
E-mail: mlangford@flsouthern.edu

Table of Contents

Florida Southern College

Analysis of Metal-Organic Framework Stability, Antimicrobial Properties, and Dental Applications

Abstract

The development of metal-organic frameworks (MOFs), an analysis of their properties, and exploration of their potential biomedical applications, specifically dental, are areas of modern biochemical interest focus on through this study. Previous research has shown these frameworks (and/or their components) have the potential for antimicrobial properties, and we hypothesized that they may be used on dental implants to inhibit the growth of oral bacteria responsible for peri-implantitis. This project has consisted of the development and structural analysis of several different novel frameworks with a high potential for microbial inhibition. Through the incorporation of antimicrobial metal ions, bridging ligands, and possibly terminal ligands there is the potential for a synergistic antimicrobial effect greater than any of the individual components. Structural stability has been monitored under varying environmental conditions, such as humidity; changes have been recorded and analyzed for potential functional applications in biological conditions. A common characteristic of MOFs is the modularity of components, which could allow for the addition of drug compounds or ligands with higher antimicrobial effects for a stronger inhibition of bacterial growth. Key MOFs were selected for antimicrobial analysis through Kirby-Bauer inhibition tests on the common oral bacteria, *Streptococcus mutans (S. mutans)*. The frameworks presenting significant bacterial inhibition were then tested for the potential of growth directly onto the titanium implants used in a majority of oral surgeries. Our research project has resulted in novel MOFs with antimicrobial properties that can be further functionalized and grown directly onto titanium implants for the prevention of infection immediately post oral surgery.

A. Project Summary

Broader Impact: Over the last several decades, oral surgeries and the placement of dental implants have improved drastically, but failure rates for implants are still at 8.16% in the maxilla and 4.93% in the mandible (Figure 1).[1] When complications and failures are considered together, the rates associated with implant-supported prostheses are as high as 24.7%.[2] Also, in demographics with preexisting medical conditions, increased age, or a suppressed immune system the failure rates are increased even further. One of the leading causes of the failure of

dental implants is the presence of infection from oral bacteria, such as *S. mutans,* shortly after surgery, leading to bone loss.[3] A class of materials that shows promise in combating this issue are metal-organic frameworks (MOFs); crystalline materials that consist of inorganic metal ions, or clusters of ions, coordinated to organic ligands for the formation of three-dimensional polymeric structures that are often porous.[4] Some MOFs have produced antimicrobial properties that would allow for the prevention of infection.[5] Within recent MOF designs there has been a synergistic effect found between the combination of multiple antimicrobial components within the framework, leading to greater bacterial inhibition.[6] The versatility of MOF structures has also allowed them to be synthesized as thin films with a consistent layer of microcrystals directly on desired surfaces through changes in reaction conditions or mechanical processing.[7] With the growth of our MOFs directly onto dental implants, commonly made of titanium, the failure rates of oral surgeries due to infections leading to peri-implantitis could be significantly reduced. Microbial inhibition would be present in the area around the implant due to the presence of the antimicrobial MOFs, with properties from sources such as the metal ions and ligand components or attached drug molecules. Also, the bactericidal properties of the MOFs in this research would allow for the elimination of *S. mutans*, preventing future, recurring infections that could materialize with bacteriostatic drugs or materials.[8] The targeted design of this series of MOFs led to systematically controlled degradation rates, which provides the potential for directed, slow-release properties that would allow for microbial inhibition to be maintained for an extended period of time.[9]

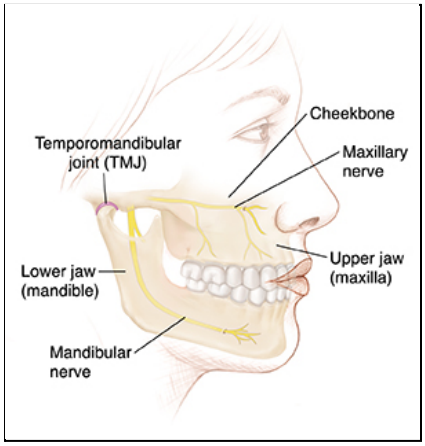

Figure 1: General Facial Anatomy. This image contains the relevant, general anatomy for the maxilla and mandible, in which the surgeries of interest would be performed.[10]

Intellectual Merit: Oral surgeries are associated with a higher risk of systemic infection due to the exposure of typically sterile areas of the oral cavity to microorganisms beyond the cutaneous barrier.[11] The current method for addressing the concern of infection with oral surgeries is through prevention and stringent protocols. A sterile surgical area is maintained through hand antisepsis, surgeon's gloves, and irrigating solutions such as sterile saline.[11] However, post-surgery no additional drugs or highly antimicrobial compounds are added unless antibiotics must be prescribed in response to an infection in the surgical site.[12,13] Instead, the sterility of the procedure is relied on to prevent future infections. It is very difficult to seal off the surgical site from all interactions with oral bacteria or microorganisms present in the environment so post-surgery complications such as peri-implantitis are frequent. Exposure to common oral bacteria, such as *S. mutans*, could cause an infection that would eventually lead to peri-implantitis and a failed implant/surgery. The antimicrobial MOFs that we have developed carry interest due to their potential use in the maintenance of a sterile location post-surgery. Their ability to be grown directly onto titanium implants will allow for prolonged prevention of bacterial growth and potentially reduced peri-implantitis rates from the moment of implant placement.

MOFs have gained interest as drug delivery systems in recent years due to their potential for high biocompatibility and effective carrying capacity of desired molecules.[14] The most common method for drug delivery using MOFs comes from their commonly porous nature and ability to interact with molecules within those pores. If the MOF is properly designed then the desired antimicrobial molecules can be associated through covalent attractions, bonding, or encapsulation. The versatility of building strategies and ease of exchanging metal ions and ligands within a MOF structure also provides them with the advantage of carrying desired materials through incorporation directly into the framework.[15] Our research will build upon prior discoveries with a focus on incorporating antimicrobial materials directly into the structure of the MOF as components of the framework and/or as terminal ligands. Instead of focusing on how to carry the antimicrobial compounds within the cavities of traditionally porous MOFs, we will focus on how to bind components, such as antibacterial drugs, as a framework and/ or auxiliary ligands.

In prior research, it has been shown that variations in the environment around specific MOFs can lead to structural variations, degradation, or the dissociation of ligands.[16,17] Due to biomedical applications of our frameworks within the oral cavity, a specific area of interest in

our research is the effect that an aqueous environment can have on the interchange of ligands and MOF decomposition. This provides our MOFs with the potential for the slow release of drugs and improved bacterial growth inhibition through their dissociation from our MOFs over an extended period of time. Within our series of MOFs, the presence of relatively high ambient humidity leads to the dissociation of MOF terminal ligands and replacement with a water molecule, leading to a more stable phase. By ensuring that the drug or antimicrobial molecule is the ligand being removed, we could extend the release of and/or enhance antimicrobial properties. We have also recorded that prolonged exposure of our MOFs to UV light leads to a change in the framework's structure and the formation of another stable MOF.[18] The effects of UV light are important to consider for the production, storage, and usage of materials in the medical field, as UV light is known to degrade several materials such as plastics and dyes. Thus, the potential for our MOFs to convert to a stable structure under UV light could allow for further applications or the protection of light-sensitive materials.[19,20] This is of increased concern in dentistry because the placement of sealants and fillings are commonly UV-cured. However, the strong presence of UV light could be used to convert our MOFs to a more stable phase with antimicrobial properties.

Not only do our compounds consist of both metal ions and associated ligands with individual antimicrobial properties, but also, more interestingly, have proven to have a synergistic effect, resulting in a greater area of inhibition and efficacy overall. The metal ion, copper(II), is well-known to have antimicrobial properties, as well as, chelidonic acid and dimethylformamide ligands (Figure 3).[21,22] These components with bacterial inhibition capabilities were specifically selected with the intention of targeting MOF production with corresponding properties. Four MOF varieties were synthesized and they all exhibited the desired synergistic antimicrobial properties by producing a statistically significant increase in *S. mutans* zones of inhibition compared to any of the individual components. (Table 8). The functionality of MOFs also allows for the replacement of ligands with desired drug compounds or strong, biocompatible antimicrobials. An interest for our frameworks would be the replacement of the pyridine ligand(s) with sulfapyridine(s) due to its known antimicrobial properties and potential to increase the synergistic effect.[21,23] We hypothesize that the unique synergistic effect may be a result of the polymeric framework degrading into fragments or chain "oligomer" segments. Rather than using the standard direct application of a single antimicrobial to prevent infection, our MOFs are capable of producing fragments of multiple antimicrobials

that can result in increased bacterial inhibition as the framework degrades. Research has shown that the synthesis of similar metal-organic assemblies occurs via the production and eventual assembly of fragments of various sizes.[24] We theorize that the degradation of our MOFs could occur in a similar pattern, although our chain polymer composition would likely break into oligomer-like pieces, with additional potential for maintaining three-dimensional associations through pi-pi stacking or hydrogen bonding (i.e., interconnecting pieces of neighboring chains). This mode of degradation would produce groupings of "blocks", which could possibly still affect the bacterial cells and induce the synergistic antimicrobial effect, instead of the dissociation of individual ligands, ions, or drugs, which do not have as great of an effect on their own even though they are the typical targets of current methods of treatment.

We have built upon the current biocompatibility research of MOFs while also producing a novel method for microbial growth inhibition and proving their relevance to the dental field. In addition, our frameworks have proven to have the capability to be grown directly onto the titanium implants commonly used in surgery.[7,25] When paired with the ability to select for framework variations and reaction conditions that will produce microcrystals, our MOFs can be added directly onto the implant and into the surgical site without inhibiting the surgical procedure. A zone of inhibition can be established as the surgical procedure is occurring and maintained throughout the healing process through a thin coating of our MOFs over the titanium implants, thus reducing the risk of peri-implantitis and failed surgeries.

B. Project Description

B.1. Research Basis

B.1.1. General Background

Since the development of MOFs in the 1990s, these compounds have gained significant research interest due to their seemingly endless potential uses (Figure 2).[26] MOFs are considered to be highly versatile materials due to the composition of their structures, potential ligand associations, and ease of functionalization of their frameworks. During the foundational studies of MOFs, researchers theorized that these structures could be applied to catalysis, gas storage, filtration, and many other applications.[27,28] However, in recent years MOF developments in the biomedical field have increased significantly, and now uses such as biomedical imaging, chemical sensors, and drug delivery are gaining focus.[27,28] Some MOFs have a very high degree of biocompatibility and multiple capacities for drug attachment/storage, which makes them a key material for directed drug delivery. Some MOFs can also be tailored for the slow or directed delivery of an associated compound through degradation or conversion of their structure. Similar to a prodrug, which requires activation from environmental compounds or conditions, MOFs can be tailored to become an active species only when placed in the appropriate location.[29] It is common for the alterations in the MOF's structure to be activated by conditions such as moisture, pH, salt-ion exchange, and others. Specifications with the encapsulating abilities of MOFs are a common focus of current research, but less emphasis is placed on the properties of materials composing the MOF providing the functionality.[30] The focus of our research was developing structures that can produce the antimicrobial properties that we desire due to the compounding effect of the structure's individual antimicrobial units (e.g., both metal ion and ligand). Since the attributes and abilities of MOFs are highly dependent on their structure, our research focused heavily on components with high antimicrobial properties. Both biocompatibility and bacterial inhibition capabilities are desirable and present in the copper metal ion, as well as, the chelidonic acid and dimethylformamide ligands.[21,22] MOFs have a highly versatile structure and the ability for auxiliary ligand binding, which provides for enhanced functionalization of their frameworks. In some instances, MOFs have extra-framework sites that have terminal ligands (i.e., non-bridging ligands) and can even be activated to have coordinatively unsaturated sites (CUSs, aka open metal sites), which occurs when there is a Lewis acid site left open on the metal ion.[31] These CUSs enhance the versatility of MOFs due to their ability to act as effective locations for potential ligand exchange or replacement.

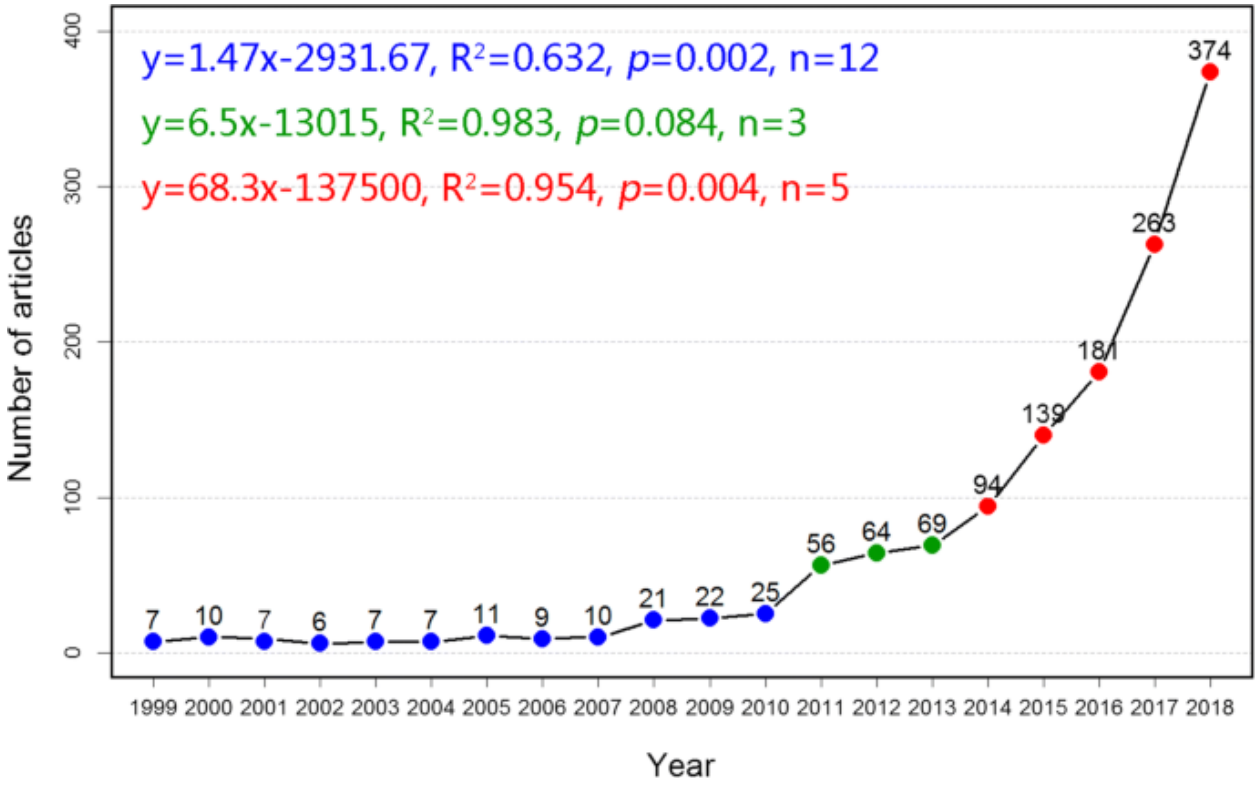

Figure 2: The trend of MOF-related articles over time.[26]

The biocompatibility and antimicrobial properties of each individual component need to be considered, as well as the MOF as a whole, due to the intent for their use *in vivo*. The focus of our research is to inhibit bacterial infections post oral surgeries and studies have shown that copper (II) would be an ideal metal ion to utilize. As such, copper (II) was selected as the central ion used in all of the MOFs we are designing or producing due to its high antimicrobial characteristics. It was found to inhibit the growth of both gram-negative and gram-positive bacteria in instances of infection.[32] It has also been shown that copper can be highly biocompatible if implemented in the appropriate manner. In high concentrations, copper can be toxic, but if diluted through methods, such as the incorporation into MOFs and slow-release, the copper concentration can produce the desired antimicrobial effects with minimal signs of toxicity.[33] Also, concerns of prolonged exposure to copper leading to toxicity can be mitigated through biodegradation. Long-term effects of copper on a biological system were tested using immersion in physiological saline and it was shown that biodegradation eventually removes copper from the system, but is maintained long enough for it to prevent infection at peak stages post-surgery.[33] Also, the versatility of MOF structures allows for the central metal ion of many frameworks to be interchangeable. Zinc metal ions, which are known to have a higher

biocompatibility than copper, have also been implemented into the reaction conditions and framework structures of our MOFs. The MOFs were shown to have antimicrobial properties and hold the potential for an even more biocompatible variation of the four main MOF structures in this study (Figure 44).

Sulfa-drugs are another component with the potential for being incorporated into our MOF structures, especially in future research, due to their well-established antimicrobial properties. In the early to mid-1900s, these compounds were directly identified for their ability to prevent or remove infections and fittingly named "miracle drugs".[34] Around the late 1930s sulfonamide had entered into dental practices and procedures for the use of preventing oral infections.[35] Sulfa-drugs are still in use in modern practices although they may have been altered as analogs or components of other medications used as antibiotics against infection.[36] Within several of our MOFs pyridine is used as a terminal ligand (Figures 3, 6, 9, 12, & 15), but without association with other compounds or conversion to derivatives, they have very little inhibitory effects on bacteria.[37] Although pyridine on its own does not present significant bacterial inhibition, the pyridine ring is present in numerous antibiotics and pharmaceuticals used in antimicrobial treatments, such as sulfapyridine (Figures 3 & 48).[23,37] By incorporating sulfapyridines into the MOF structure instead of pyridines as the terminal ligands, we can, in theory, maintain a consistent structure while improving the compounding antimicrobial properties. Sulfa-drugs have been labeled as biocompatible since the 1900s and in modern studies sulfapyridine has been used to treat conditions such as rheumatoid arthritis, thus reaffirming the biocompatibility of this particular drug.[38] Finally, metal-organic frameworks have proven to be biocompatible and are already in use within several organic-biological systems. For instance, different MOF compounds have been developed for therapeutics, drug carriers, and numerous other applications.[39,40]

For our research project, components such as titanium implants, thin film growth, and *S. mutans* (as the model bacteria) were selected for application testing once the novel MOFs had been properly developed. Titanium implants are the material of choice in nearly all oral surgeries due to their biocompatibility, resistance to corrosion, and mechanical properties.[41] In an effort to replicate the environment and materials that our MOFs would be nucleated onto prior to an oral surgery, we decided to use titanium implants as well. Variations in crystal size or morphology could carry varying antimicrobial effects and impact the MOF's interactions with the titanium implant or biological environment.[42] One method that may increase the concentration of MOF

growth directly onto titanium implants is the use of thin films. Thin film growth will allow for the functionalization of the surface of the implant, but the crystal size of only a few nanometers will not inhibit the implant's function.[7,43] Depending on the MOF variant, numerous methods for influencing thin film growth have been established. Some MOFs can be run in large batch conditions and still produce thin films, while others may require layering, growth onto surfaces, secondary addition, or other factors.[44] Thin film growth's ability to occur directly onto the desired surface, such as titanium, allows for a very efficient process. The last, crucial component to the application testing of our novel MOFs is the bacteria that they will be tested against for efficacy. *S. mutans* was the selected pathogenic bacteria due to its high prevalence within the oral cavity and common involvement in infections post-surgery leading to peri-implantitis.[45,46]

Several research studies prior to ours found that MOF structures may experience compositional changes, degradation, or stability alterations under varying conditions that are present in a biological setting.[47,48] In some instances degradation could be the desired method for the release of materials and directed application of compounds in a biological system. In other research studies, the structural variations have led recent researchers to explore more water-stable MOFs and/or MOFs that do not vary with the environment.[17,49,50] Understanding the stability of a MOF could allow for better-tailored delivery of materials or standardized efficacy, so studies involving the effects of humidity, chemicals, temperature, and UV light are highly beneficial. The effects of water absorption on the retention of structure and surface area in MOFs is a crucial factor to consider due to the placement of our structures within the oral cavity. It has been shown through powder x-ray diffraction (PXRD) analysis that the metal ion's strength of interactions with its associated ligands and other available molecules in the environment plays a key role in the stability of the MOF structure when exposed to high humidity.[17] The metal nodes of MOFs are prime locations for the catalysis of reactions, ligand displacement, or open site interaction with environmental compounds/molecules.[51] Dependent on the metal ion, which is copper (II) in all of our MOFs, and the ligands it has within its coordination sphere, frameworks can be tailored for desired degradation or stability within an aqueous environment.

Most metals are Lewis acids, which indicates that the copper (II) metal ion of our structure, will have an increased tendency to accept a water molecule when placed in an environment with high humidity (unless otherwise protected; e.g., sterics). Thus, the structure of our MOF, the strength of its ligand interactions, and the reaction conditions it is developed in will have to be used to dictate how it responds to humidity in the local environment. A central

metal ion is also heavily involved in how a MOF responds to chemical and thermal alterations. The more inert a central metal ion is and the greater the steric hindrance around it, the lower the effect of chemical and thermal conditions.[52] Zeolite-like MOFs (ZMOFs) are known to have extreme stability in high heat and acid-base conditions due to their association with large ligands and often a high specific surface area.[53] The studies referenced indicate that in varying thermal conditions, the metal-ligand binding within the MOF can carry a more significant effect on its stability than the metal ion alone. Another factor that can affect the stability of MOFs, is UV light due to its tendency to cause degradation, compositional changes, or additional bonding to the already present framework.[54] This finding carries significance with the preparation of our compounds and the placement of sealants and fillings, which are commonly UV-cured. Either UV exposure could be avoided to maintain the composition of our intended MOF or the UV-altered structure could provide the benefit of a stable antimicrobial alternative.

The production of novel MOFs is a significant factor in this research project, but they also need to be identified and tested for reproducibility and efficacy. The tools used for analysis include PXRD, infrared spectrometry (IR), thermogravimetric analysis (TGA), and single-crystal x-ray diffraction (SCXRD). PXRD is a highly versatile analysis tool and it can be used for the identification of compounds, purity analysis, tracing degradation, and identifying the conversion between structures. A PXRD instrument measures the diffraction pattern of crystalline material and produces a series of peaks dependent on the structure of its crystal lattice.[55] IR can also be used for the identification of structures, as well as the interpretation of the bonds composing it. IR uses the interactions between infrared light and the molecule to identify functional groups. If the overall composition of the molecule, or in the focus of MOFs, crystal is known, then the IR data can be used to confirm the binding of desired components and relative molecular arrangement.[56] A thermogravimetric analyzer is used to evaluate the thermal stability of a structure by recording the weight change as the heat is increased at a constant rate.[57] In the consideration of MOFs, TGA can be used for the analysis of stability, decomposition rates, composition, and solvent/ ligand loss. Single-crystal x-ray diffraction provides an extensive amount of information in regards to the internal crystal lattice of a structure. A large portion of this information is essential in understanding the 3D composition of a MOF, such as bond angles, bond length, and molecular arrangement.[58] Through the use of numerous instruments and analysis techniques the identification, properties, and application testing of our novel MOFs can be accomplished.

B.2. Results

B.2.1. Methods and Materials

All chemicals were used as purchased. MOF reactions were conducted using the conditions presented in Tables 1, 2, 3, and 4. Single-crystal x-ray diffraction data was collected on Bruker AXS diffractometers at the University of South Florida, the University of Florida, and Florida Gulf Coast University (FGCU). Powder x-ray diffraction was conducted using a Bruker D_2 Phaser CCD diffractometer at Florida Southern College. Kirby Bauer testing was performed using Mueller Hinton media and sample placement directly onto the agar.

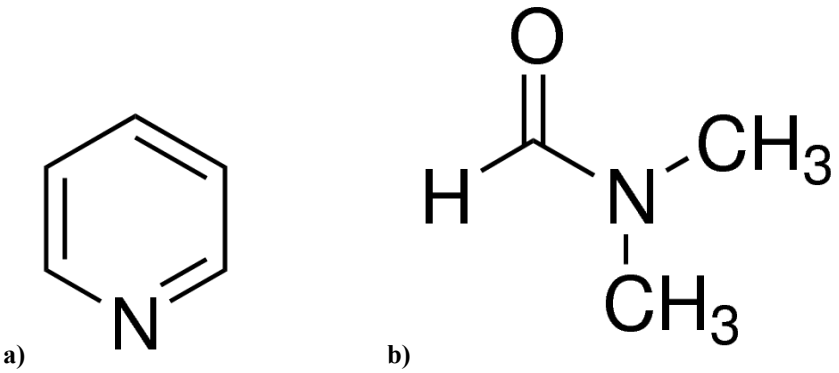

Figure 3: Ligands in MOF Production. a) Pyridine molecular structure[59] and b) N,N-dimethylformamide molecular structure[60]

B.2.2. Metal-Organic Framework Structures

Four main MOF phases were produced through the reaction conditions presented below (Table 1). It is important to note that for many of the phases fresh DMF (bottled within the last month) is required for proper crystal development. Through single crystal data analysis, calculated values for each framework were established, which allowed for confidence in the identification and reproduction of each MOF. PXRD diffractograms were used in comparison with the calculated PXRD from single-crystal values for the determination of the MOFs. Single crystal data also allowed for the production of 3D molecular structures in crystal structure software for the analysis of bonding, molecular arrangement, and interactions between chains. Without magnification, the crystal structure of different MOFs may appear similar, but the proper magnification can allow for the identification of differences in shape, color, and size.

- **Phase 1**

  $[Cu_2(CDO)_2(pyr.)_4(H_2O)_2]_n$

Table 1: Reactions Conditions for 1

Metal	Ligand	Solvents	Temperature
0.04mmol $Cu(NO_3)_2 \cdot 2.5H_2O$	0.04mmol $H_2CDO \cdot 1H_2O$	2.0mL DMF	85℃, 24hrs
		1.0mL EtOH	
		0.1mL pyr	

Alternative reaction conditions: Through the addition of 0.1mL of DI water to the **2**, **3**, and **4** reaction conditions, the humidity-stable phase, **1**, is produced**.**

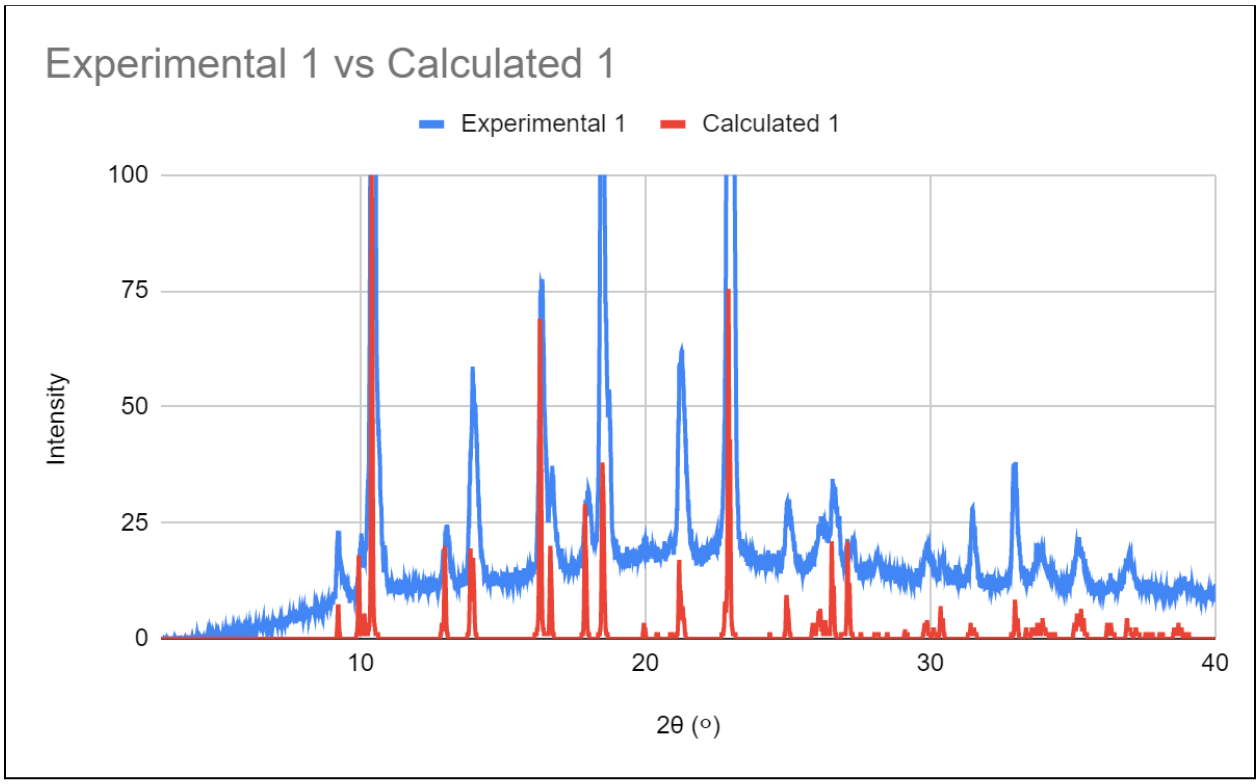

Figure 4: PXRDs of Experimental 1 vs Calculated 1. As can be seen in the diffractogram, the experimental PXRD peaks align well with the calculated peaks from single crystal analysis. Thus, indicating that the appropriate structure has been produced and replication of **1** was successful.

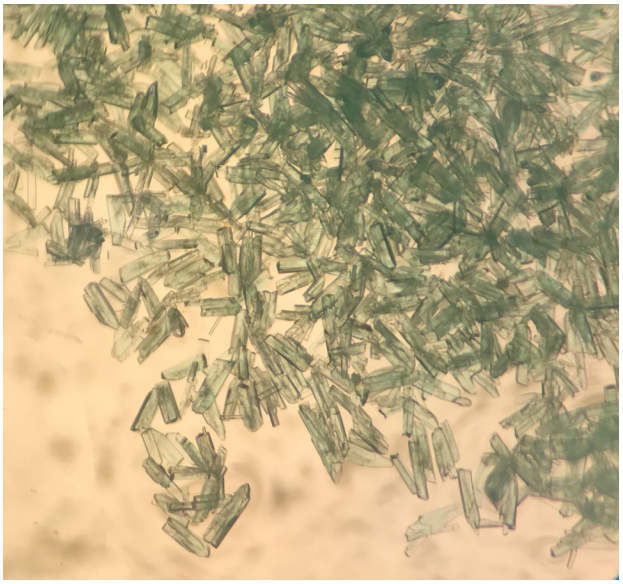

Figure 5: Microscopic image of 1 (100x). The crystals of **1** are larger, rod-shaped, contain defined edges and angles, and have a light blue coloration.

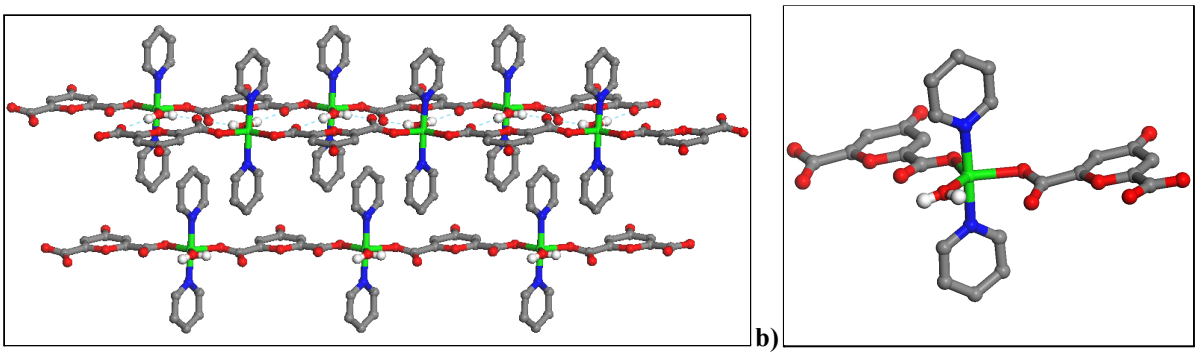

Figure 6: Molecular structure of 1. a) A portion of three chains from the structure of **1** (the final humidity-stable phase). Light blue lines (faint) between the upper two chains show the hydrogen bonding, horizontal association between chains for the orientation above. Pi-pi stacking can be observed between the upper and lower chains, allowing for the vertical association between chains in the orientation above. b) The molecular building block (MBB) of **1** with two nitrogen atoms and three oxygen atoms as the coordination (CuN_2O_3) around each copper ion (Cu^{2+}). This figure shows the trigonal bipyramidal structure with two pyridine terminal ligands and one water molecule terminal ligand per copper metal ion. Some hydrogen atoms have been omitted for clarity; C = gray, O = red, N = blue, Cu = green.

- **Phase 2**

  $[Cu_2(CDO)_2(DMF)_2(pyr.)_4]_n$

Table 2: Reaction Conditions for 2

Metal	Ligand	Solvents	Temperature
0.04mmol $Cu(NO_3)_2 \cdot 2.5H_2O$	0.04mmol $H_2CDO \cdot 1H_2O$	3.0mL DMF	85℃, 24hrs
		0.1mL pyr	

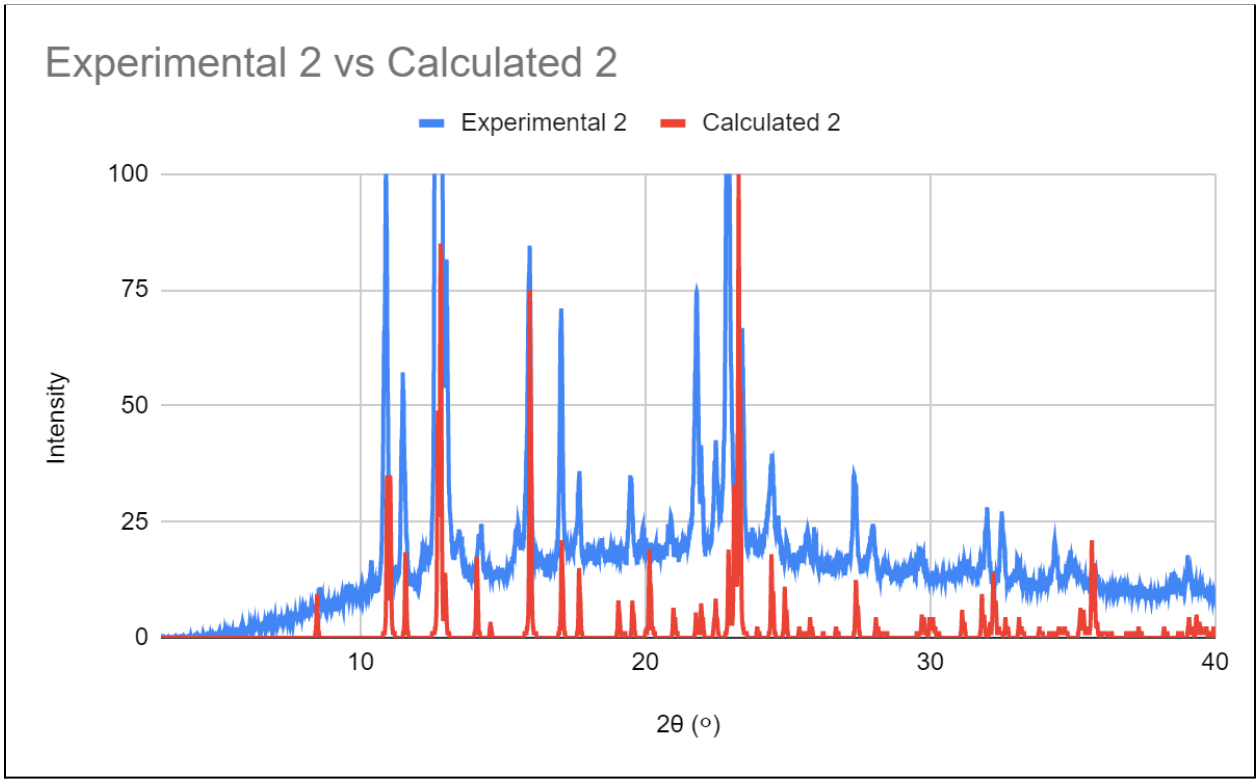

Figure 7: PXRDs of Experimental 2 vs Calculated 2. As can be seen in the diffractogram, the experimental PXRD peaks align well with the calculated peaks from single crystal analysis. Thus, indicating that the appropriate structure has been produced and replication of **2** was successful.

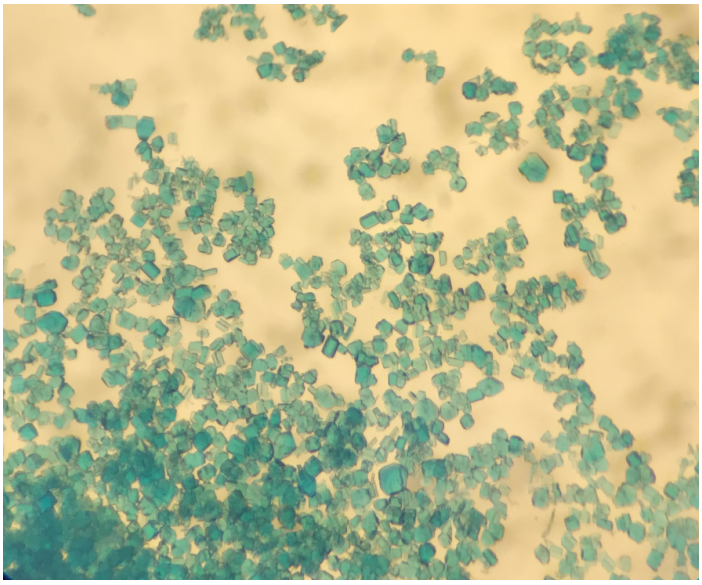

Figure 8: Microscopic image of 2 (100x). The crystals of **2** are larger, cubic-like polyhedral shape, and a light blue (though darker) coloration. Without the microscope, **1** and **2** can have very similar coloration and appearance.

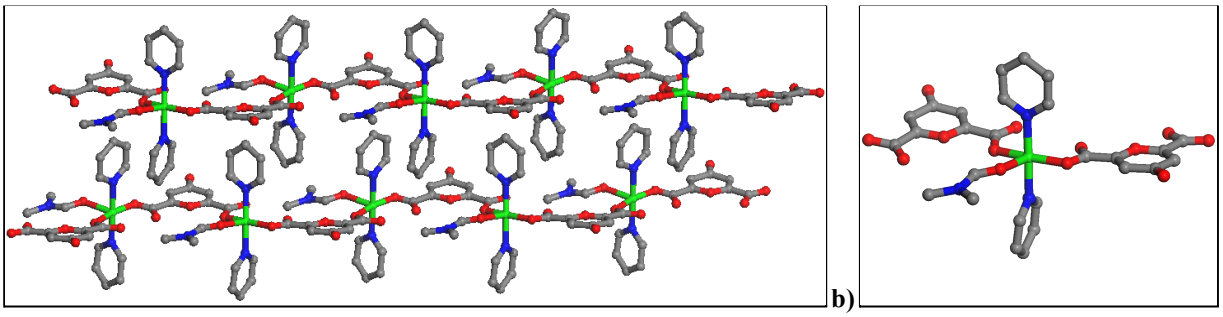

Figure 9: Molecular structure of 2. a) Portions of two chains from the structure of **2**. Pi-pi stacking is present between the upper and lower chains, allowing for the vertical association between chains for the orientation above. b) The MBB of **2** with two nitrogen atoms and three oxygen atoms as the coordination (CuN_2O_3) around each copper ion (Cu^{2+}). This figure shows the square bipyramidal structure of **2** with two pyridine terminal ligands and one DMF terminal ligand per copper metal ion. Some hydrogen atoms have been omitted for clarity; C = gray, O = red, N = blue, Cu = green.

- **Phase 3**

  $[Cu_2(CDO)_2(DMF)(pyr.)_5]_n$

Table 3: Reaction Conditions for 3

Metal	Ligand	Solvents	Temperature
0.04mmol $Cu(NO_3)_2 \cdot 2.5H_2O$	0.04mmol $H_2CDO \cdot 1H_2O$	2.0mL DMF	85℃, 24hrs
		0.1mL pyr	

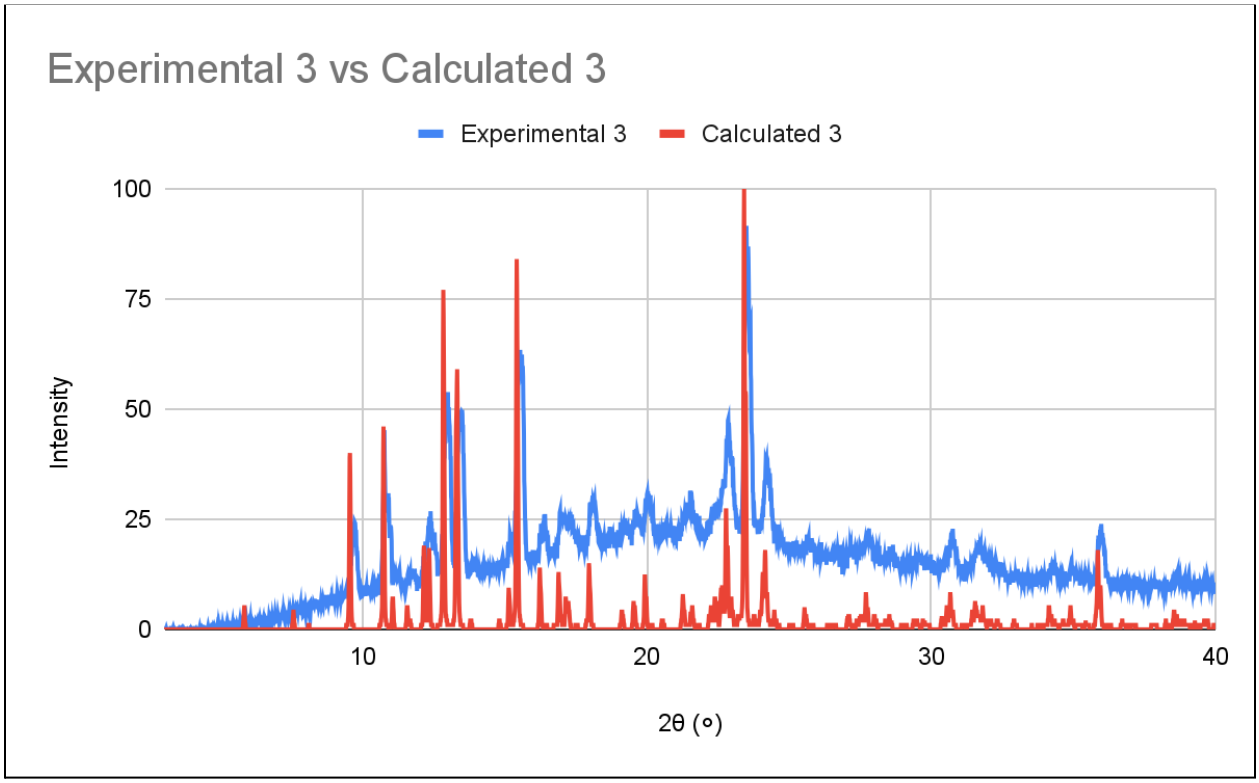

Figure 10: PXRDs of Experimental 3 vs Calculated 3. As can be seen in the diffractogram, the experimental PXRD peaks align well with the calculated peaks from single crystal analysis. Thus, indicating that the appropriate structure has been produced and replication of **3** was successful.

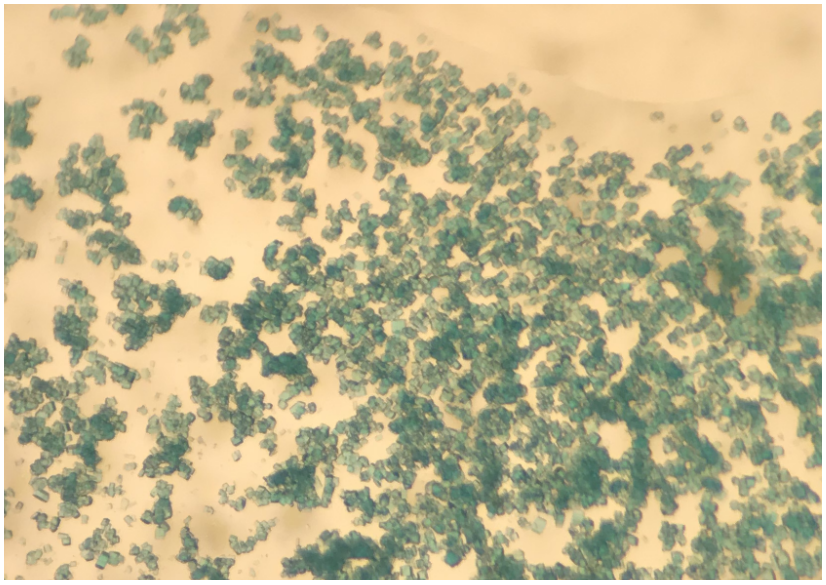

Figure 11: Microscopic image of 3 (100x). The crystals of **3** are moderately smaller, with defined sides and edges, and a dark blue coloration.

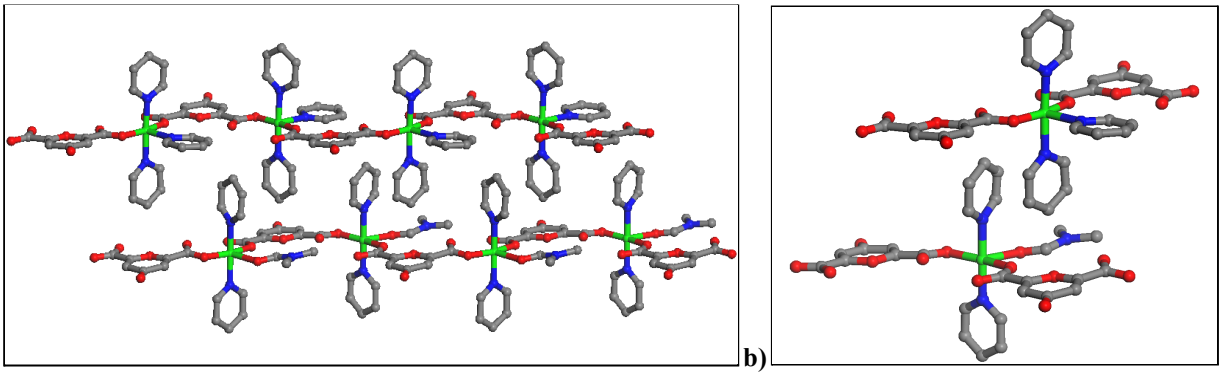

Figure 12: Molecular structure of 3. a) A portion of each type of single-chain (there are two independent chain types) from the structure of **3**. Pi-pi stacking is present between the upper and lower chains, allowing for the vertical association between chains for the orientation above. b) The MBBs from each chain, with either two nitrogen atoms and three oxygen atoms (CuN_2O_3) or three nitrogen atoms and two oxygen atoms (CuN_3O_2) as the coordination around each copper ion (Cu^{2+}), respectively. This figure shows the square bipyramidal structure with terminal ligands of pyridine and DMF. Within the two chain variants, one chain has three pyridine terminal ligands per copper metal ion, while the other chain has two pyridine terminal ligands and one DMF per copper metal ion. Some hydrogen atoms have been omitted for clarity; C = gray, O = red, N = blue, Cu = green.

- **Phase 4**

  $[Cu_2(CDO)_2(pyr.)_6]_n$

Table 4: Reaction Conditions for 4

Metal	Ligand	Solvents	Temperature
0.04mmol $Cu(NO_3)_2 \cdot 2.5H_2O$	0.04mmol $H_2CDO \cdot 1H_2O$	2.0mL DMF	85℃, 24hrs
		0.8mL pyr	

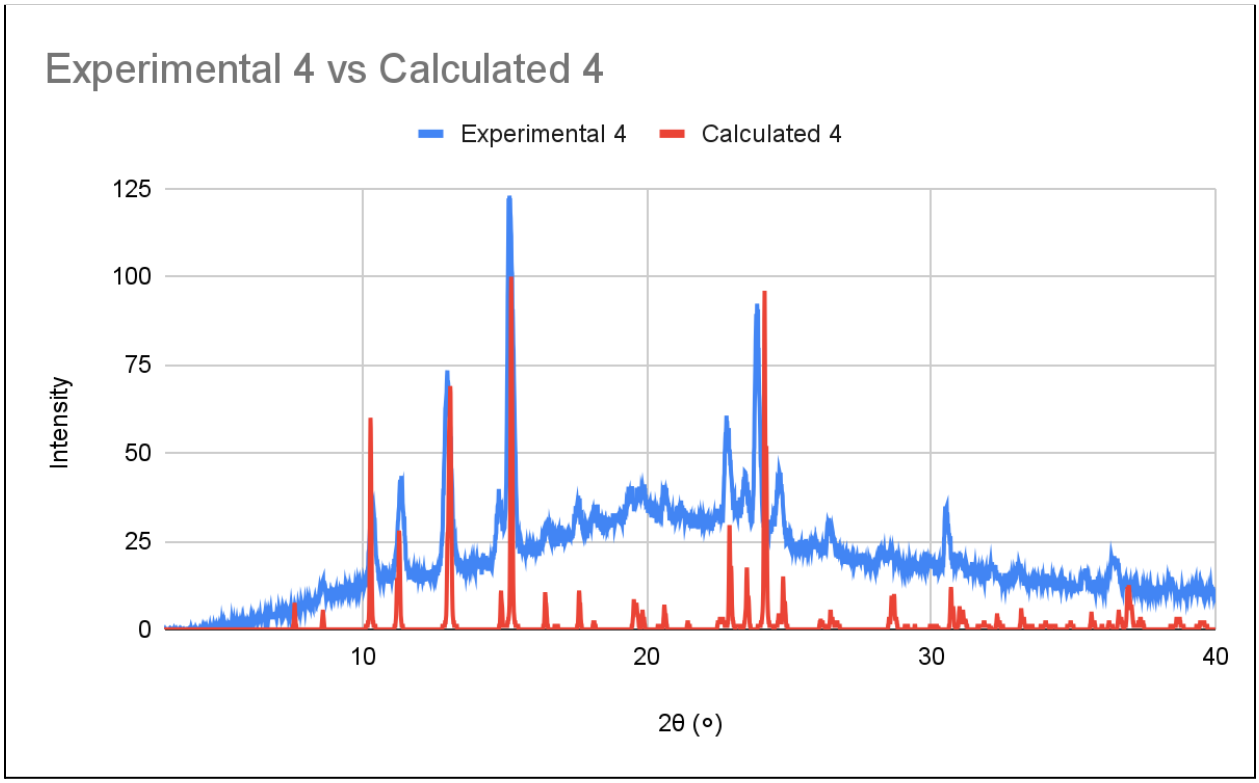

Figure 13: PXRDs of Experimental 4 vs Calculated 4. As can be seen in the diffractogram, the experimental PXRD peaks align well with the calculated peaks from single crystal analysis. Thus, indicating that the appropriate structure has been produced and replication of **4** was successful.

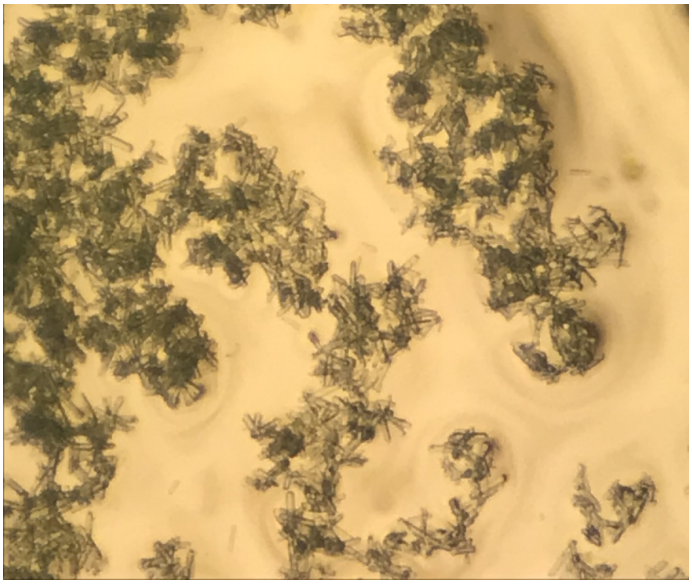

Figure 14: Microscopic image of 4 (100x). The crystals of **4** are microcrystals, spindle/geometric shaped, and a lighter blue/green coloration.

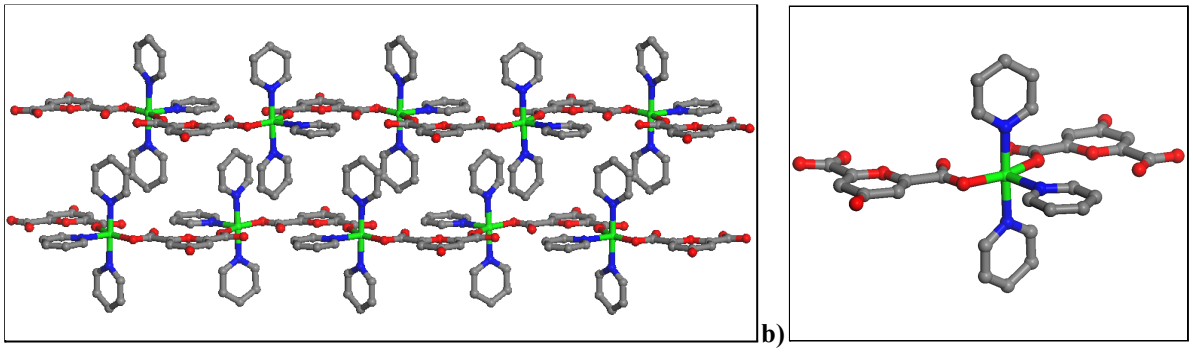

Figure 15: Molecular structure of 4. a) A portion of two chains from the structure of **4.** Pi-pi stacking is present between the upper and lower chains, allowing for the vertical association between chains for the orientation above. b) The MBB with two nitrogen atoms and three oxygen atoms as the coordination (CuN_2O_3) around each copper ion (Cu^{2+}). This figure shows the trigonal pyramidal structure of **4** with three pyridine terminal ligands per copper metal ion. Some hydrogen atoms have been omitted for clarity; C = gray, O = red, N = blue, Cu = green.

B.2.3. MOF Purity without Chelidonic Acid Crystals

Chelidonic acid (H_2CDO/CDO) is only partially soluble in some of our solvents at room temperature and thus carries the ability to recrystallize once a reaction is complete, so PXRD analysis was needed to ensure that unassociated H_2CDO was not present in our MOF products. The purity of our MOFs was determined through a comparison between the calculated PXRD, experimental PXRD, and a PXRD of H_2CDO monohydrate crystals. There were no peaks that align with H_2CDO without also aligning with the calculated PXRD. Thus the MOFs did not contain any H_2CDO crystal impurities.

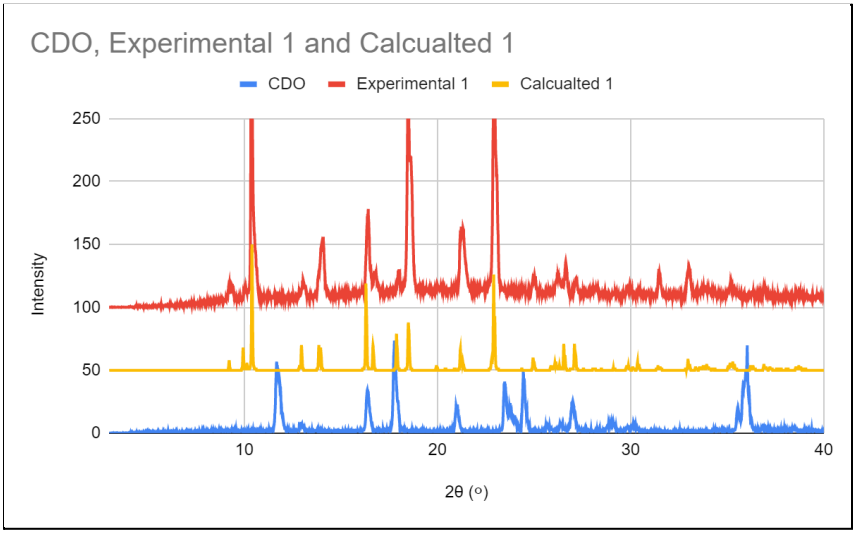

Figure 16: Comparision of CDO Crystals, Experimental 1, ad Calculated 1. The PXRD diffractograms above show a comparison between CDO crystals, experimental **1**, and calculated **1**. The experimental **1** PXRD lacks any significant/obvious CDO crystal PXRD peaks that are not also present in the calculated **1** PXRD. This indicates that the experimental MOF crystals are pure, without reformed CDO crystal contamination.

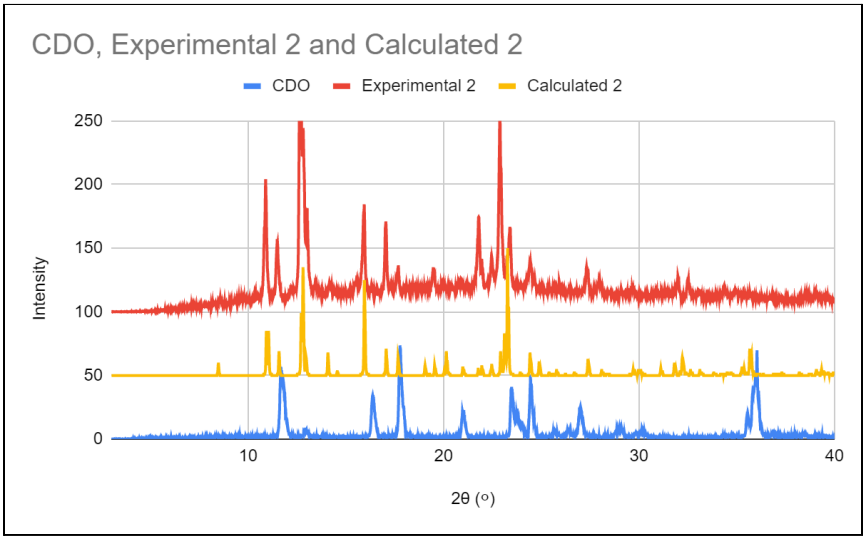

Figure 17: Comparision of CDO Crystals, Experimental 2, ad Calculated 2. The PXRD diffractograms above show a comparison between CDO crystals, experimental **2**, and calculated **2**. The experimental **2** PXRD lacks any CDO crystal PXRD peaks that are not also present in the calculated **2** PXRD. This indicates that the experimental MOF crystals are pure, without reformed CDO crystal contamination.

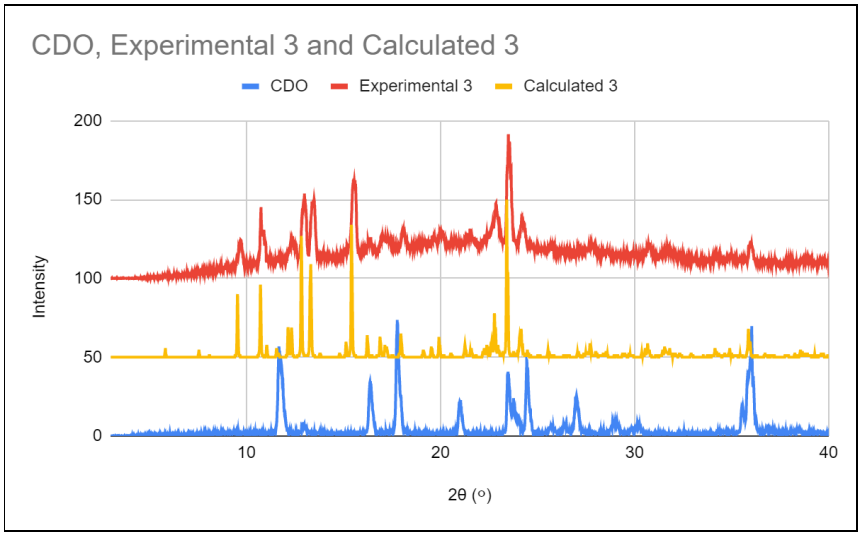

Figure 18: Comparision of CDO Crystals, Experimental 3, ad Calculated 3. The PXRD diffractograms above show a comparison between CDO crystals, experimental **3**, and calculated **3**. The experimental **3** PXRD lacks any CDO crystal PXRD peaks that are not also present in the calculated **3** PXRD. This indicates that the experimental MOF crystals are pure, without reformed CDO crystal contamination.

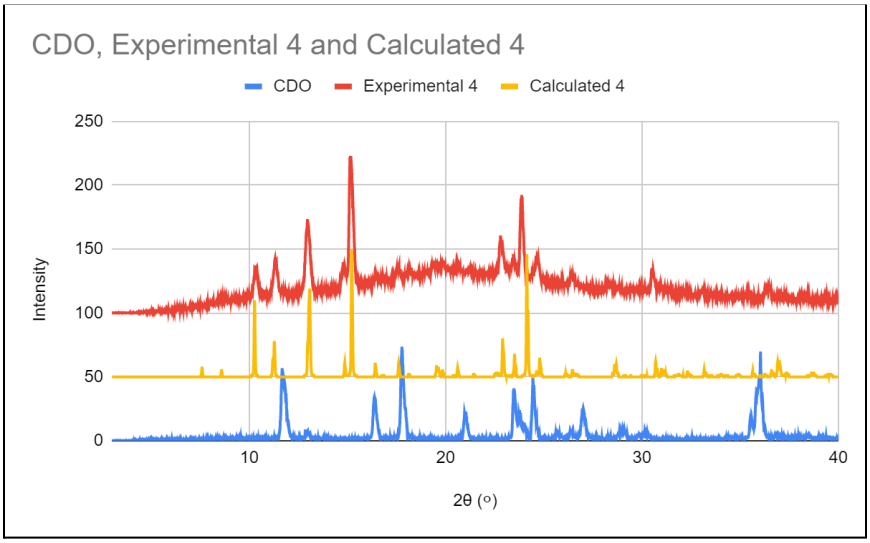

Figure 19: Comparision of CDO Crystals, Experimental 4, ad Calculated 4. The PXRD diffractograms above show a comparison between CDO crystals, experimental **4**, and calculated **4**. The experimental **4** PXRD lacks any CDO crystal PXRD peaks that are not also present in the calculated **4** PXRD. This indicates that the experimental MOF crystals are pure, without reformed CDO crystal contamination.

B.2.4. Humidity Testing

A unique phenomenon was observed for phases 2-4. After a short period of time running the PXRD, each was observed to change color. Upon color change, the PXRD was run again, and the diffractogram had changed significantly, in fact, all subsequently matched **1**. To determine whether this was a result of exposure to x-ray or light, the samples were left on the bench (instead of under x-ray), but the color and diffractogram pattern still changed. Similarly, when

left in the dark, the samples still changed. This suggested that neither x-rays nor ambient light were the cause. It was noted that **1** is the only structure with coordinated water, and we theorized that due to the high relative humidity in the laboratory environment, **2**-**4** absorbed moisture to convert to **1**. As such, MOF humidity testing was used to determine the stability of **2**, **3**, and **4** and their conversion rates to **1** in environmental conditions of 20- 21.67℃ and 58- 63% relative ambient humidity. Each framework was placed on a PXRD plate and then a succession of scans was obtained until the diffractograms showed full conversion to **1**. The primary scan of each MOF was used for its identification through comparison with the single-crystal data. In order to accomplish a scan without **2**, **3**, or **4** beginning conversion to **1** the sample had to be placed damp (with the mother solution), thus leading to relatively high background in the first scan of each series. The differences in peak intensity and time required for full conversion were then used to determine conversion rates and stability.

Figure 20: Experimental **2** on a PXRD plate immediately after plating.

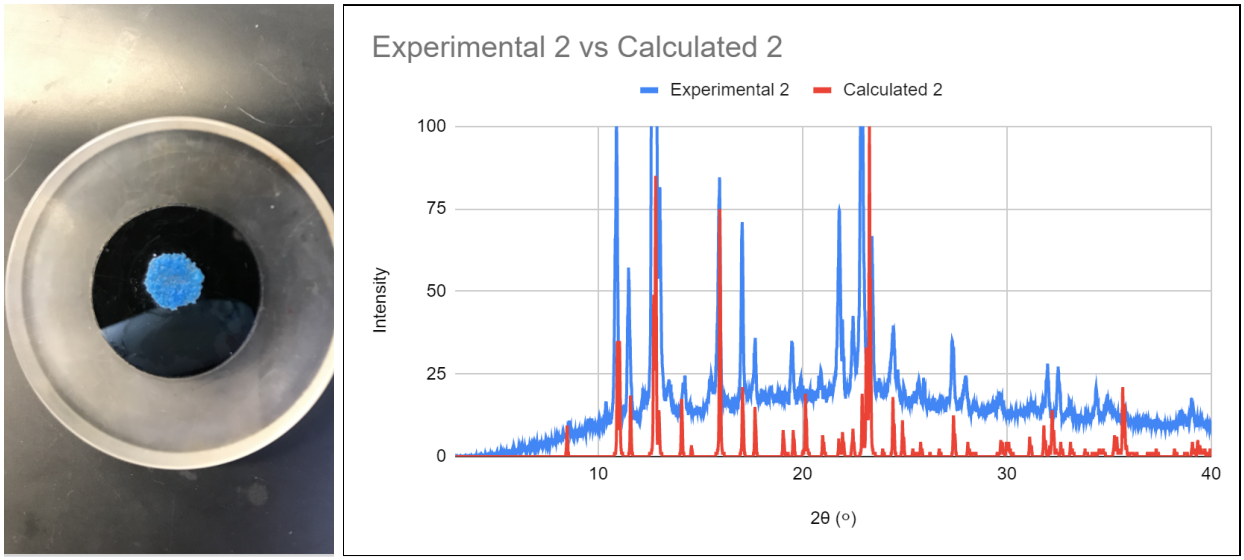

Figure 21: The first PXRD of Experimental **2** (Run 1, 10 minutes).

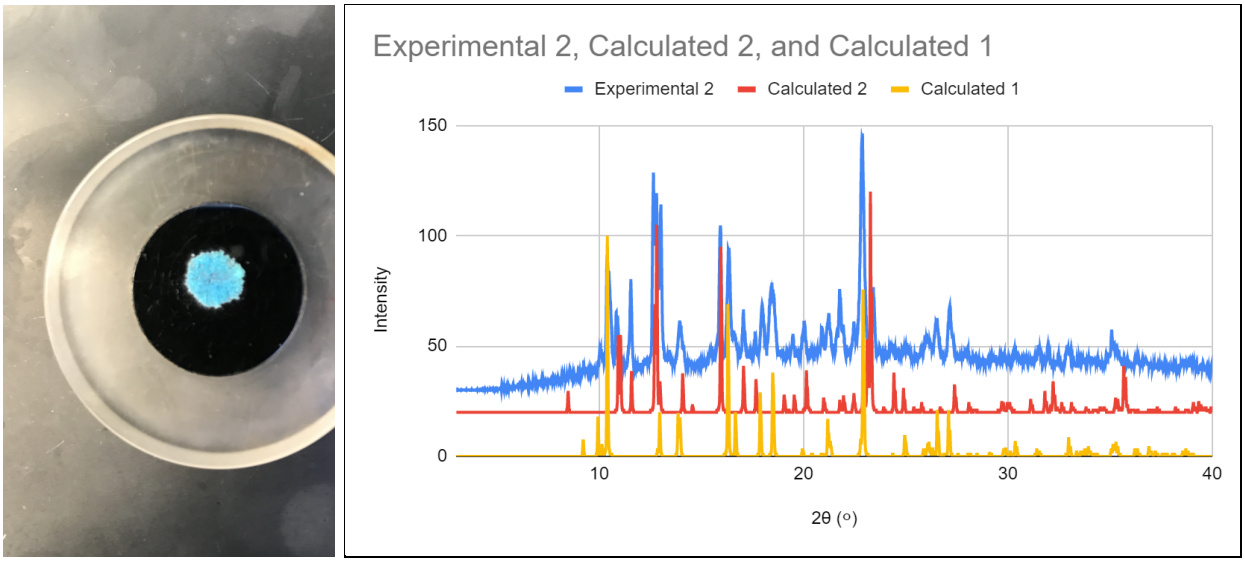

Figure 22: Run 2 of Experimental 2, 20 minutes

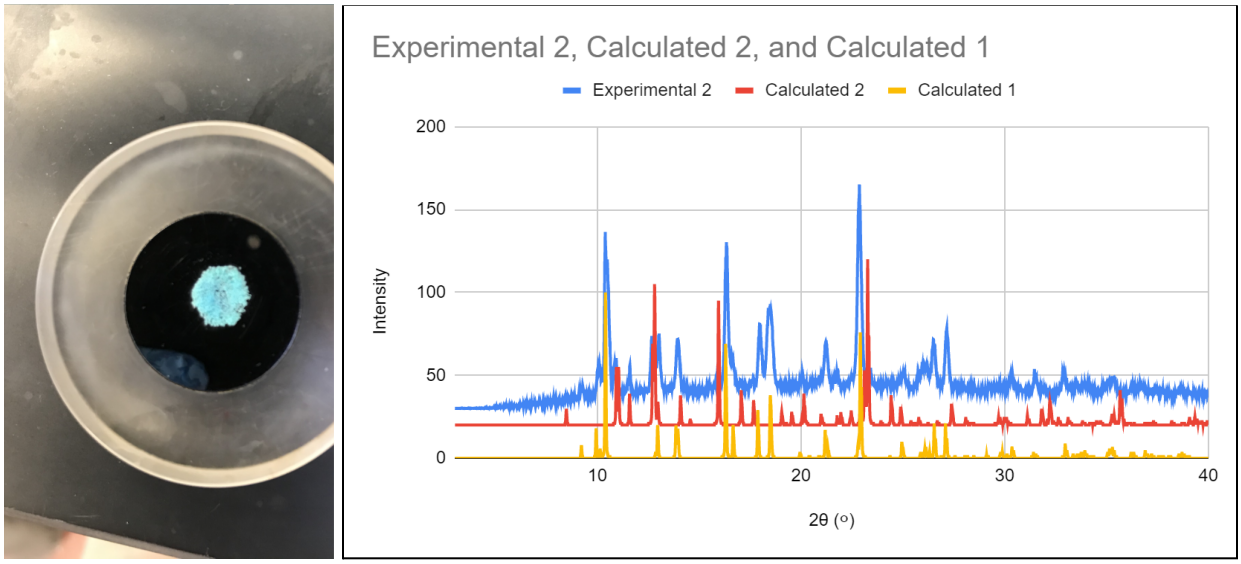

Figure 23: Run 3 of Experimental 2, 30 minutes

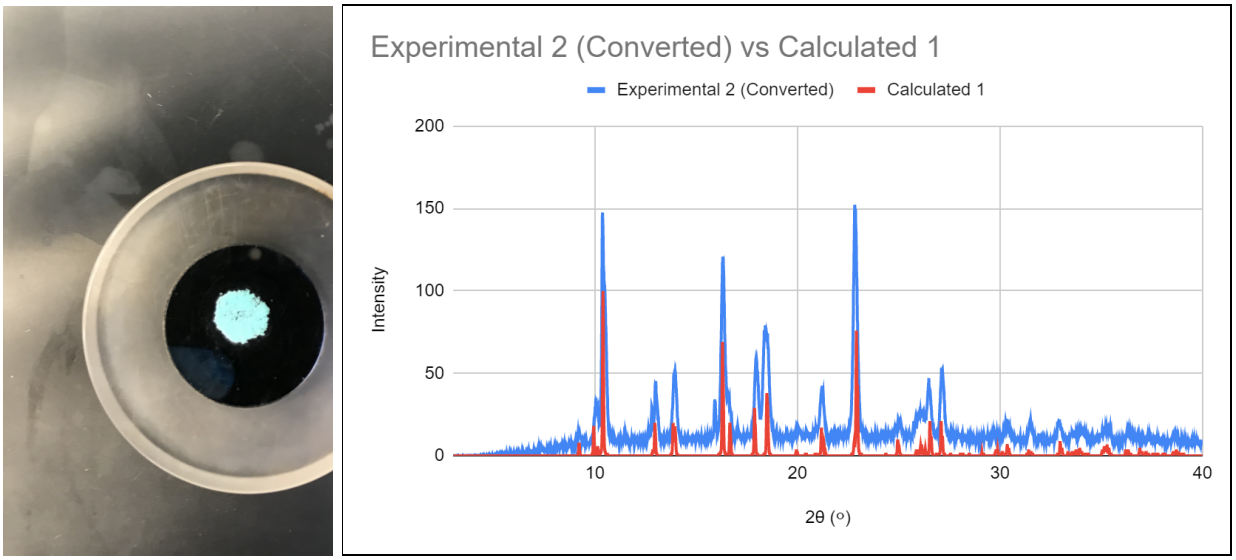

Figure 24: Run 4 of Experimental 2 (Converted), 40 minutes

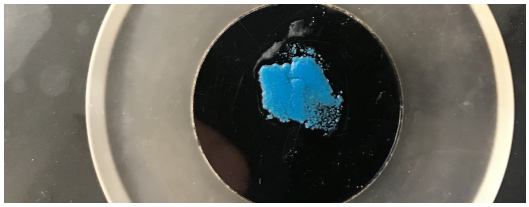

Figure 25: Experimental 3 on a PXRD plate immediately after plating.

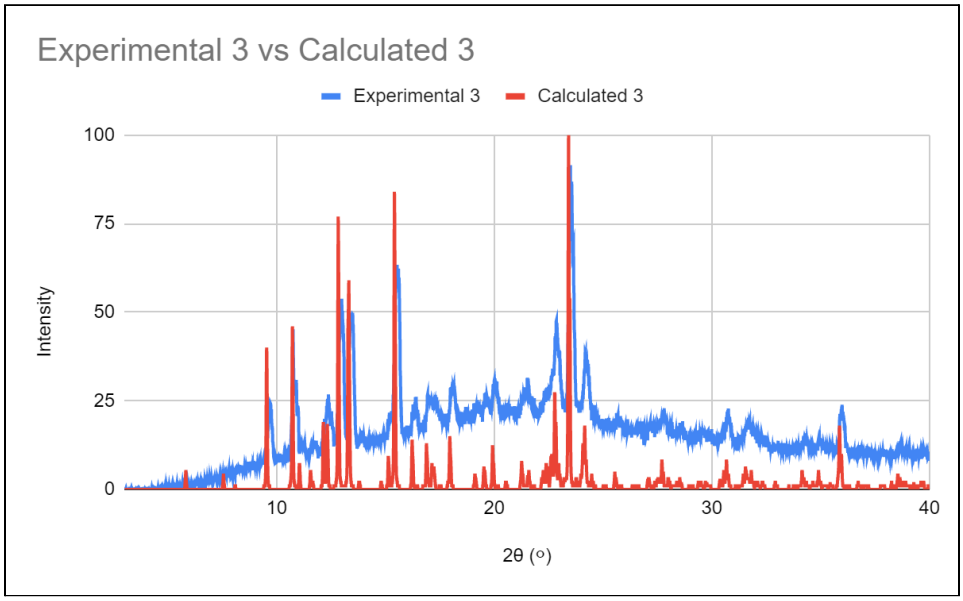

Figure 26: The First PXRD of Experimental 3.

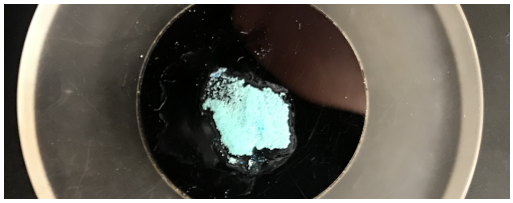

Figure 27: Experimental 3 on a PXRD plate after run 10 (106 minutes).

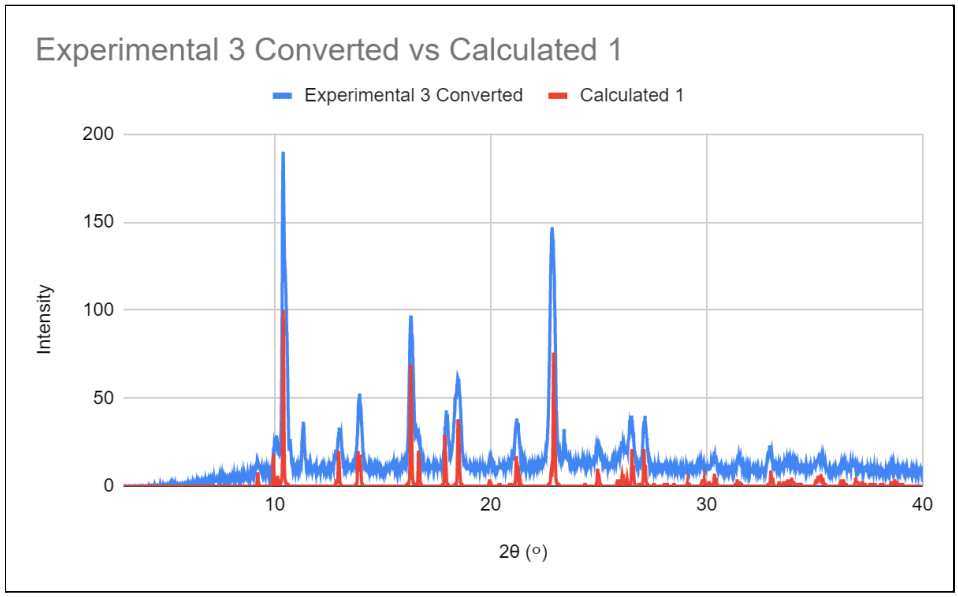

Figure 28: The 10th PXRD of Experimental 3, after conversion to 1

Figure 29: Experimental 4 on a PXRD plate immediately after plating.

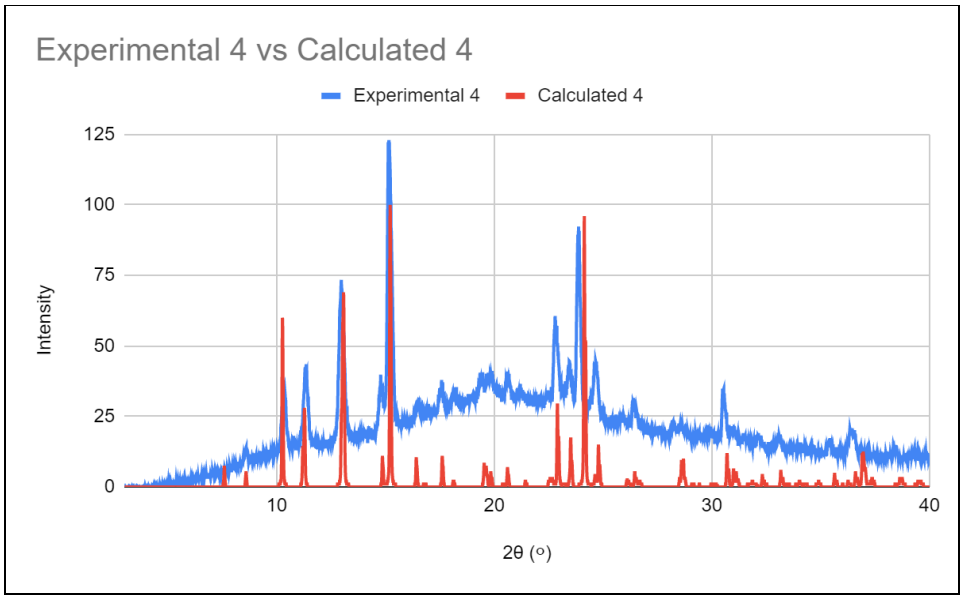

Figure 30: The First PXRD of Experimental 4.

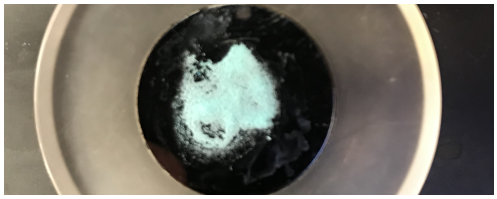

Figure 31: Experimental 4 on a PXRD plate after run 6 (61 minutes).

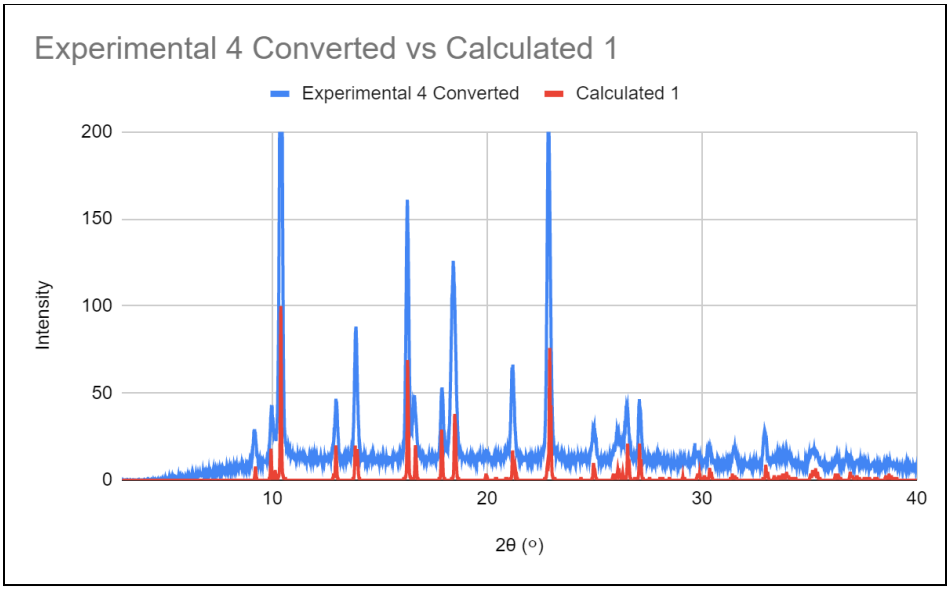

Figure 32: The 6th PXRD of experimental 4, after conversion to 1

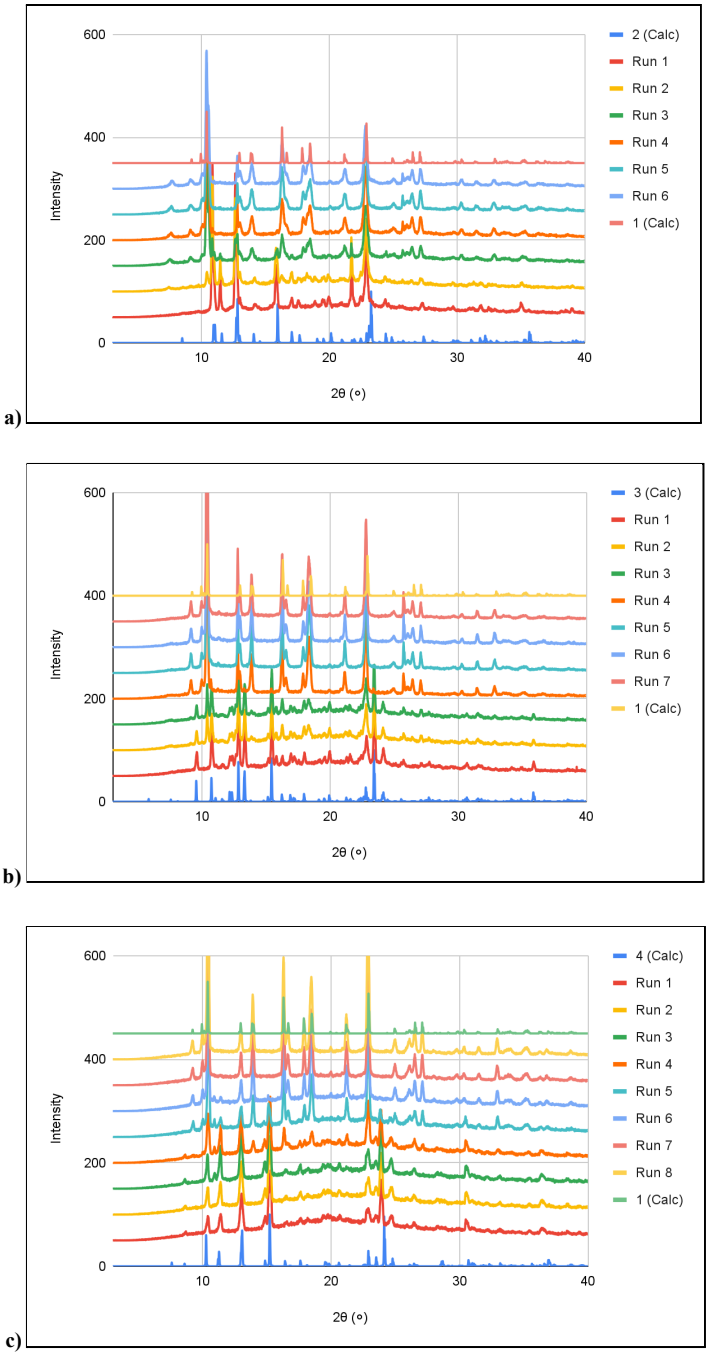

Figure 33: PXRD of single-crystal-to-single-crystal phase changes. a) Compound **2** to compound **1** transformation (~62 min); b) compound **3** to compound **1** transformation (~72 min); c) compound **4** to compound **1** transformation (~82 min).

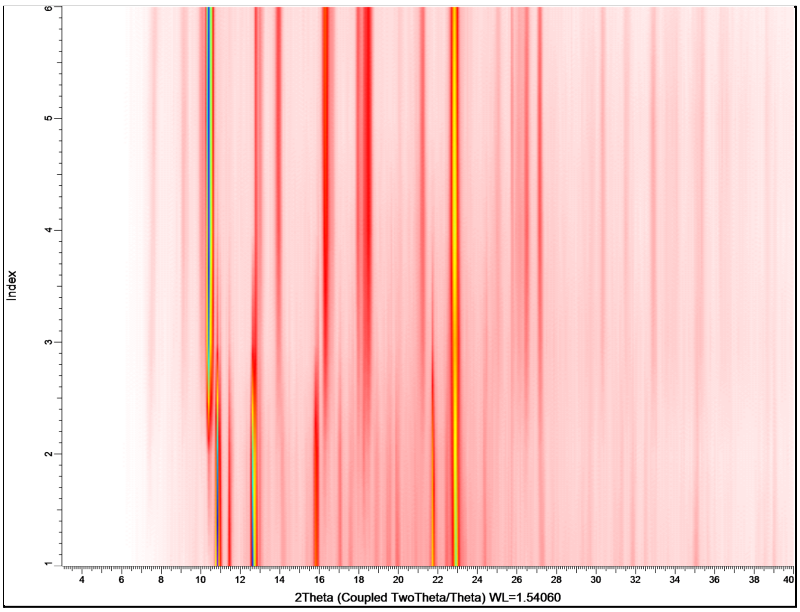

Figure 34: 2D Graph of 2 Humidity Conversion. The figure above shows peak expression intensity over time. The graph should be ready from bottom to top, with the bottom representing the starting peaks and the top representing peaks after a series of PXRD scans and MOF conversion. Using PXRD scans, the gradual diminishment of the peaks indicative of **2** can be seen and the intensity of **1**'s peaks increases significantly. Some peaks, such as at 23 2Θ, are consistent in both structures.

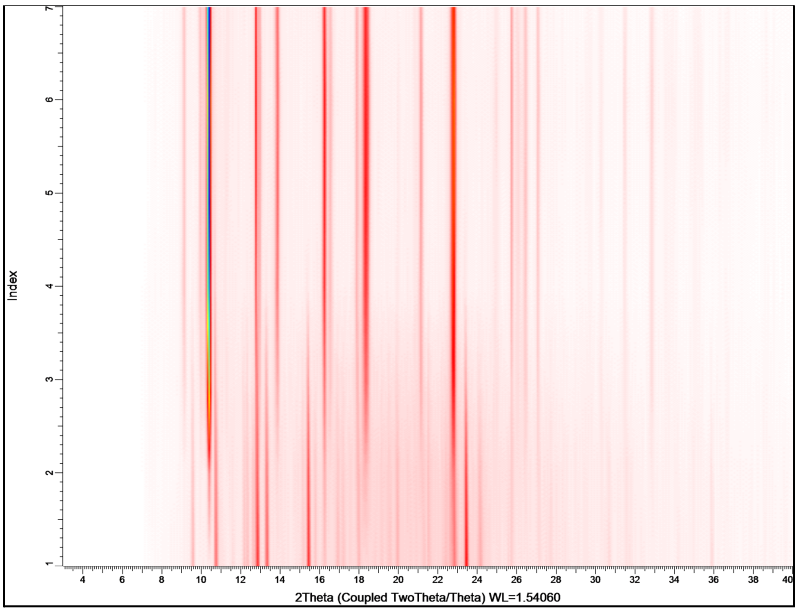

Figure 35: 2D Graph of 3 Humidity Conversion. The figure above shows peak expression intensity over time. The graph should be ready from bottom to top, with the bottom representing the starting peaks and the top representing peaks after a series of PXRD scans and MOF conversion. Using PXRD scans, the gradual diminishment of the peaks indicative of **3** can be seen and the intensity of **1**'s peaks increases significantly. Some peaks, such as at 23 Two Theta, are consistent in both structures.

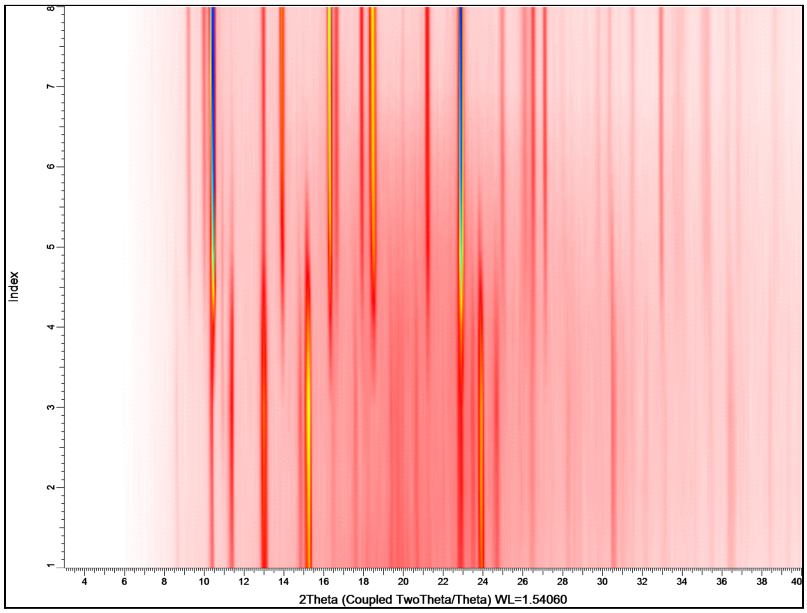

Figure 36: 2D Graph of 4 Humidity Conversion. The figure above shows peak expression intensity over time. The graph should be ready from bottom to top, with the bottom representing the starting peaks and top representing peaks after a series of PXRD scans and MOF conversion. Using PXRD scans, the gradual diminishment of the peaks indicative of **4** can be seen and the intensity of **1**'s peaks increases significantly. Some peaks, such as at 23 Two Theta, are consistent in both structures.

Table 5: Conversion Rates of 2, 3, and 4 to 1. For MOFs **2**, **3**, and **4** a prominent PXRD peak was selected that did not share any overlap with the calculated peaks of **1** (Two Thetas of **2**- 10.844°, **3**- 23.528°, **4**- 15.157°). For **1** the prominent PXRD peak at 10.397° was selected which is not shared with the PXRDs of the other three MOFs. The relative magnitude of each peak was calculated as a percentage of the maximum peak magnitude at the indicated 2θ (°) out of all of the PXRDs for each MOF. Relative conversion rates can then be analyzed through the decreasing or increasing peak height in relation to the maximum. Note: Due to the background causing an average deviation between 10-15 on the y-axis intensity, 15 was subtracted from every value prior to the calculation of peak percentages. Also, only one peak was chosen for the calculation of rates. As a result, the chosen peak may reach 0% or 100% prior to full conversion of the MOF due to the presence of other PXRD peaks that are still increasing or decreasing.

Minutes	**2**	**1**		**3**	**1**		**4**	**1**
12	100%	0%		100%	0%		100%	9.94%
22	71.99%	7.89%		82.31%	0%		100%	10.80%
32	12.36%	78.22%		79.74%	32.38%		100%	15.00%
42	2.29%	90.28%		53.10%	60.92%		96.97%	22.93%
52	0%	94.24%		26.23%	75.96%		50.24%	42.08%
62	0%	100%		17.75%	97.99%		13.47%	65.72%
72				0%	100%		5.36%	84.66%
82							0%	100%

B.2.5. Submersion in DI Water Testing

Due to the apparent stability of **1**, especially in humid environments and a variety of solvent systems, crystals of **1** (via Method 1) were also submerged in DI water and monitored by PXRD after exposure to the aqueous environment.

a)
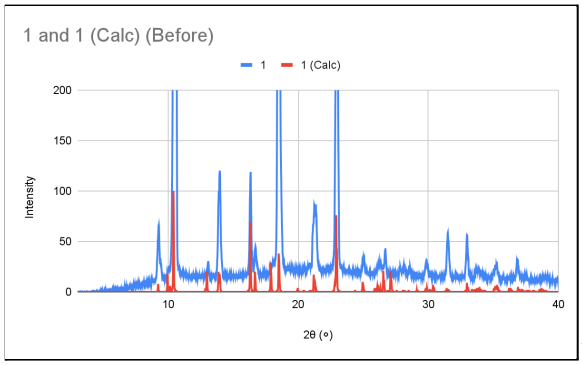

b)
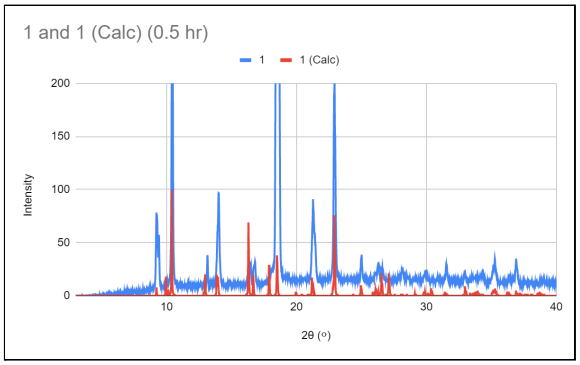

c)
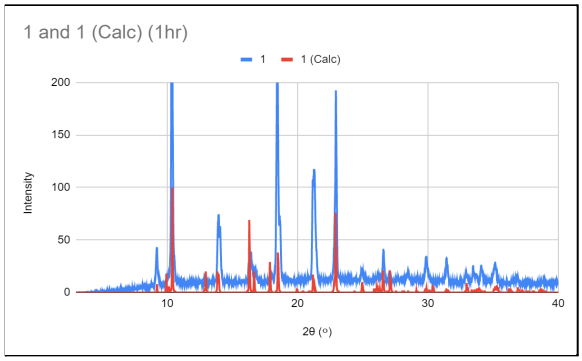

d)
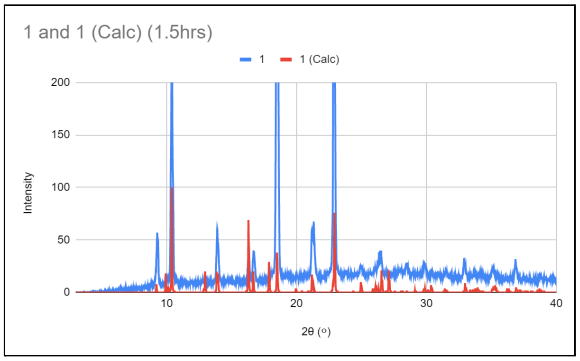

e)
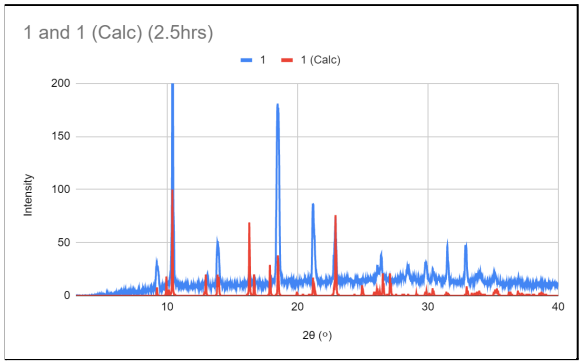

f)
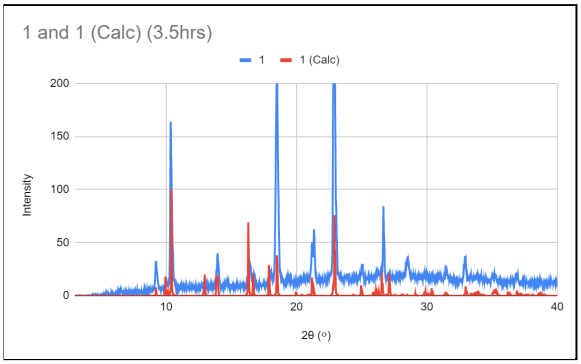

g)
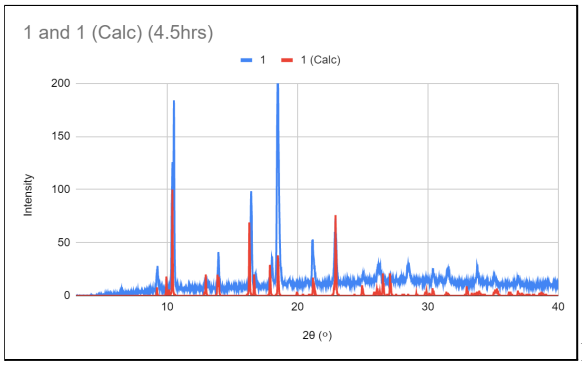

h)
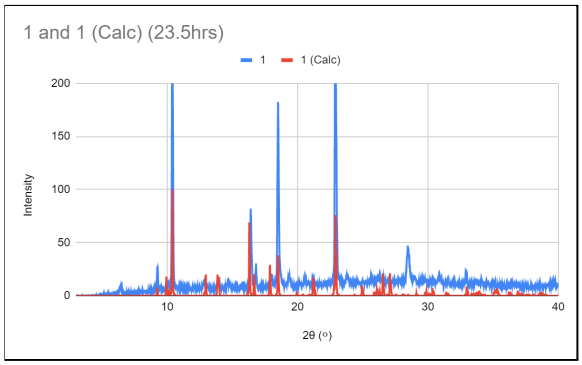

i) 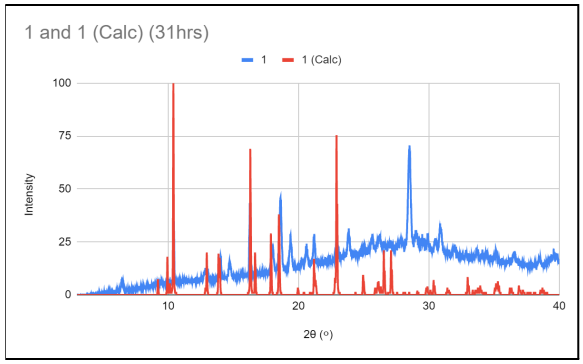

Figure 37: PXRDs of 1 upon exposure to aqueous solution. a) Before submersion in DI water b) 0.5 hrs post submersion c) 1.0 hr post submersion d) 1.5 hrs post submersion e) 2.5 hrs post submersion f) 3.5 hrs post submersion g) 4.5 hrs post submersion h) 23.5 hrs post submersion i) 31 hrs post submersion

B.2.6. UV Testing

Through prolonged exposure to UV light, approximately one week, the composition of all four main MOFs will convert to a more stable phase. The UV phase was of interest due to its potential applications associated with its increased stability and maintained antimicrobial properties. PXRDs were run to confirm the conversion of the four main frameworks to the UV phase.

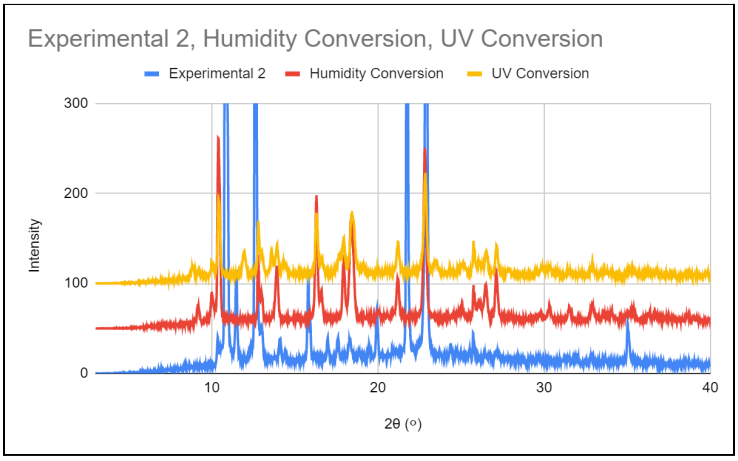

Figure 38: UV conversion testing. This figure shows the PXRDs of the initial structure of **2**, the structure of the humidity stable phase, **1**, after humidity conversions, and the framework structure after UV conversions.

B.2.7. Kirby-Bauer Testing

The Kirby-Bauer testing for all compounds was performed on Mueller Hinton media plates and the samples were placed directly onto the agar. A McFarland Test Standard was used to produce consistent *S. mutans* growth on all plates through a suspension of the bacteria in a 0.9% saline solution until the opacity was comparable against a Wickerham card to the Hardy Diagnostics standard vial of McFarland latex 0.5.[61] Using a funnel 6mm in diameter, an average mass of 0.00813g of MOFs **1**, **2**, **3**, and **4** were placed with each sample as determined by five sample weight tests. **1** was tested under three conditions; only the dry MOF, the MOF washed in ethanol, and the MOF in its mother solution. MOFs **2**, **3**, and **4** were only placed in their mother solutions due to their lack of stability once removed from the solution. Using the average MOF mass of 0.00813g the dependent mass of each individual component was calculated, using mole to mole ratios, to be directly proportional to their composition within the frameworks. Copper (II) nitrate hemipentahydrate was placed at 0.00446g. Chelidonic acid was placed at 0.00353g. The liquid samples, pyridine, DMF, and ethanol, were placed at 20µL due to the average amount of mother solution placed with the samples in mother solution. The mother solutions of **1**, **2**, **3**, and **4** were also tested without any frameworks present at 20µL due to the average amount of mother solution placed with samples in the mother solution.

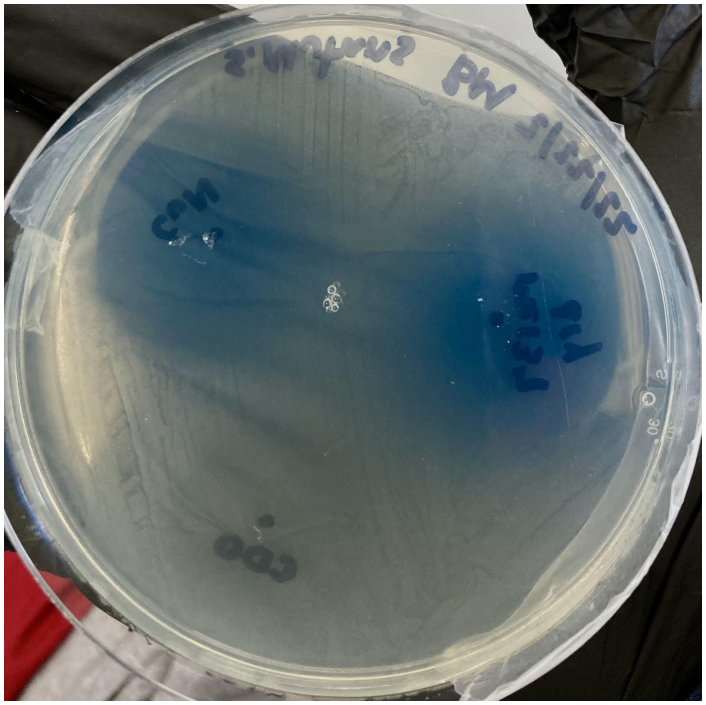

Figure 39: $Cu(NO_3)_2$, 1, and H_2CDO. The zones of inhibition in this image are $Cu(NO_3)_2$ in the top left, **1** with no solution (dry) in the top right, and H_2CDO in the bottom center.

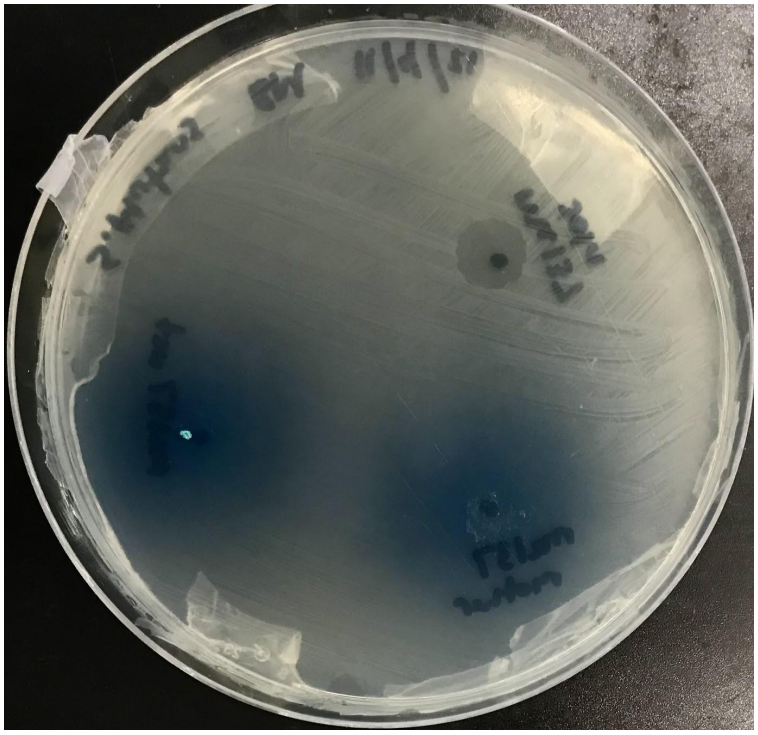

Figure 40: 1 (EtOH wet), 1 (mother soln.), 1 Solution. The zones of inhibition in this image are **1** from a solution of EtOH on the left, **1** from its mother solution in the bottom right, and only the mother solution of **1**, with no crystals, in the top right.

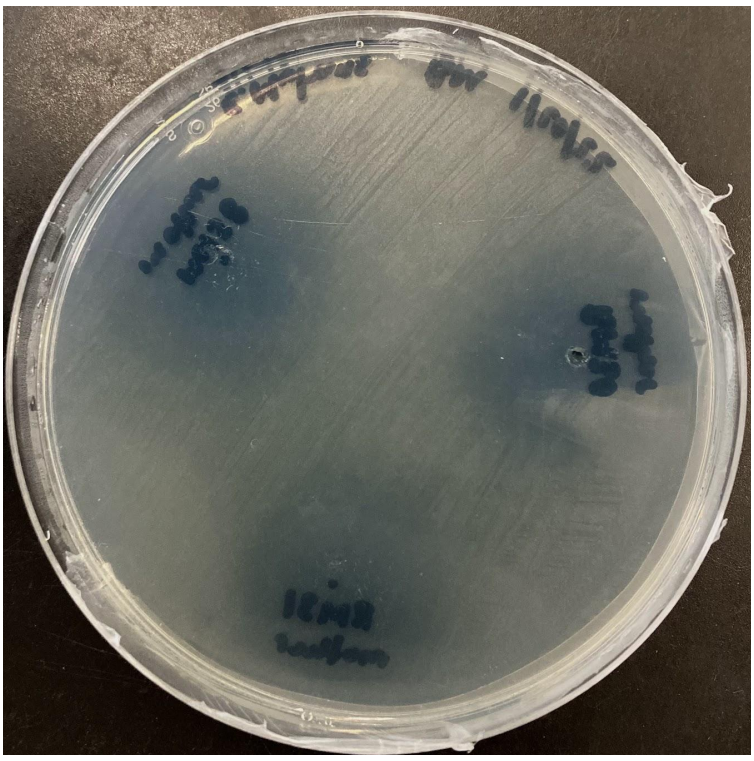

Figure 41: 2 (mother soln.), 3 (mother soln.), 4 (mother soln.). The zones of inhibition in this image are **2** from its solution on the right, **3** from its mother solution in the top left, and **4** from its mother solution in the bottom.

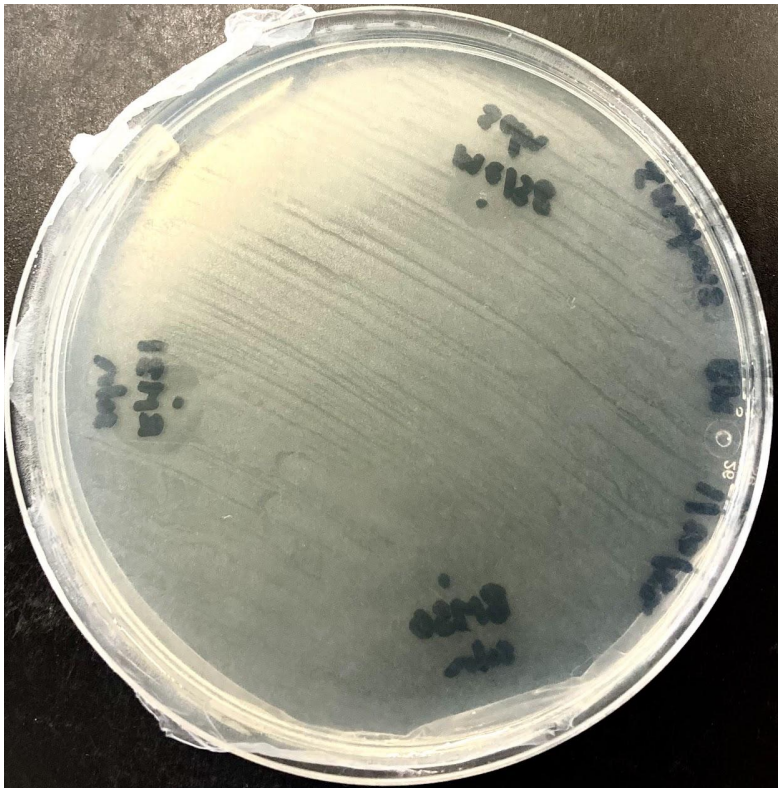

Figure 42: 2 solution only, 3 solution only, 4 solution only. The zones of inhibition in this image are **2** mother solution only on the bottom right, **3** mother solution only in the top right, and **4** mother solution only on the left.

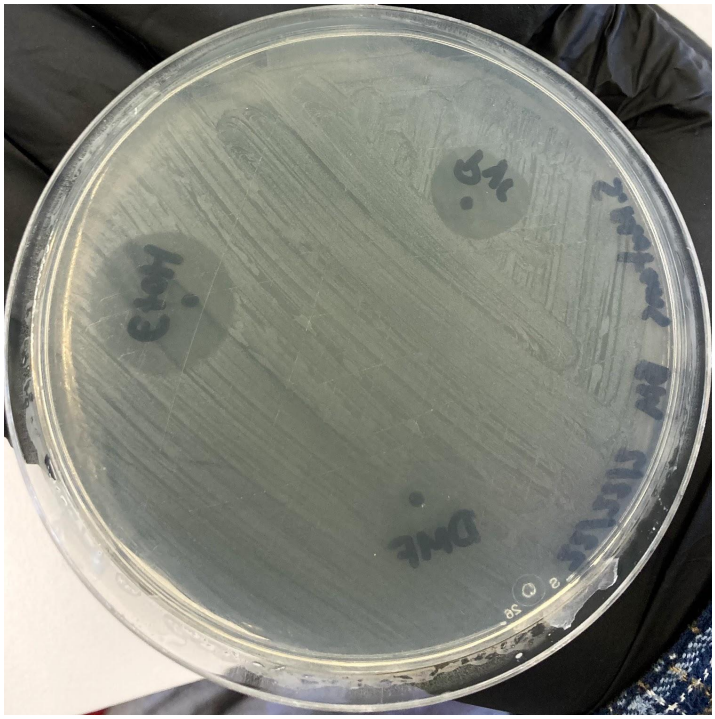

Figure 43: EtOH, Pyr., DMF. The zones of inhibition in this image are ethanol on the left, pyridine in the top right, and dimethylformamide in the bottom right.

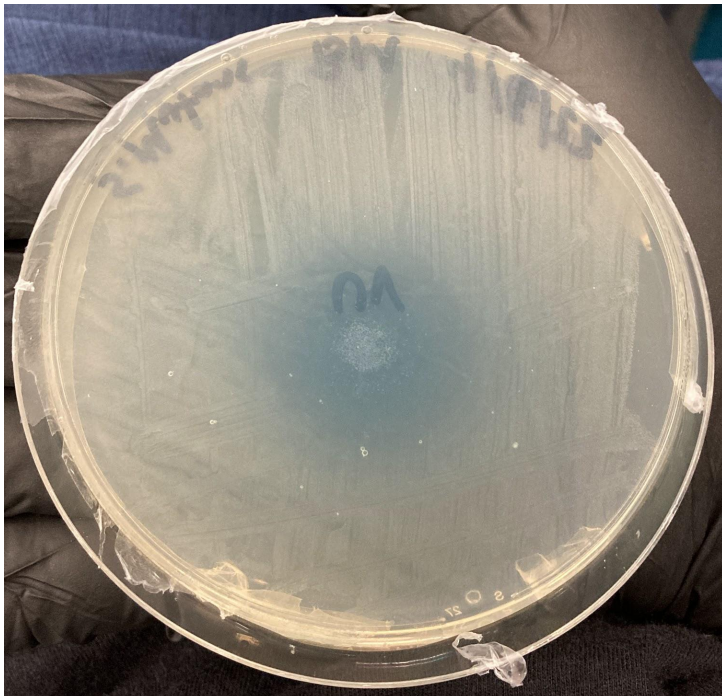

Figure 44: UV Converted 1. The center zone of inhibition in the image above is the UV Conversion of **1** at 25mm.

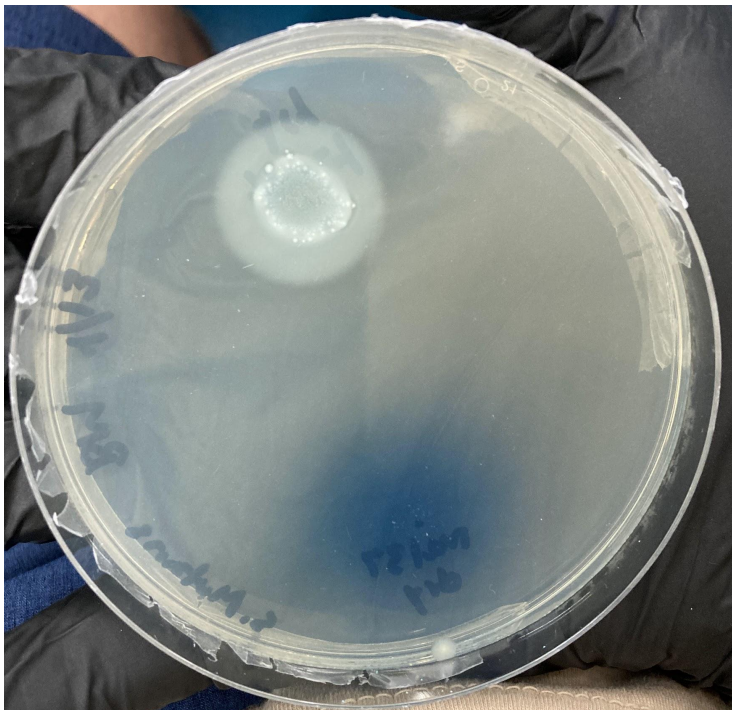

Figure 45: Zinc Experimental vs 1. The zones of inhibition in this image are the zinc experimental (Dry) at 28mm (top) and **1** (Dry) at 32mm (bottom).

Table 6: Reaction Conditions for Zinc Experimental

Metal	Ligand	Solvents	Temperature
0.04mmol $Zn(NO_3)_2.2.5H_2O$	0.04mmol $H_2CDO{\cdot}1H_2O$	1.0ml DEF	50℃, 24hrs
		1.0ml MeOH	
		0.1ml pyr	

Table 7: Average Zones of Inhibition. This table shows the average zones of inhibition of the four framework phases, their solutions, and the components involved in each framework's reaction. Four full trials were completed with inhibition results for every sample. Note: Only the results from complete trials are included in this table. Individual tests or multiple tests of 1 (Dry) and CuN are included in Table 8 for statistical significance.

	Test 1	**Test 2**	**Test 3**	**Test 4**	**Average (mm)**
1 (EtOH wet)	23	30	37	32	**30.5**
1 (Dry)	22	25	35	30	**28**
1 in mother soln.	23	24	36	32	**28.75**
2 in mother soln.	25	28	32	31	**29**
3 in mother soln.	22	25	34	34	**28.75**
4 in mother soln.	21	27	30	36	**28.5**
1 soln. only	8	16	12	11	**11.75**
2 soln. only	8	16	9	11	**11**
3 soln. only	7	15	11	9	**10.5**
4 soln. only	9	16	10	11	**11.5**
CuN	20	27	30	25	**25.5**
H_2CDO	15	21	20	21	**19.25**
Pyr.	11	17	15	10	**13.25**
EtOH	17	19	18	17	**17.75**
DMF	7	10	7	10	**8.5**

Table 8: A) Data and B) Unpaired T-Test. Table A above shows the data of nine Kirby-Bauer tests of **1** dry (**1** (Dry)) and copper (II) nitrate (CuN). In order to increase certainty in the statistical analysis of these data sets a larger number of trials were used. Table B provides the results of an unpaired T-test between **1** dry and copper (II) nitrate to determine if their zones of inhibition are significantly different. The nine zone of inhibition values of **1** dry (M= 27.89, SD= 4.46) compared to the nine of inhibition values of copper (II) nitrate (M= 23.33, SD= 4.53) demonstrated that **1** dry had significantly larger zones of inhibition, $t(16)= 2.1512$, p= 0.0471.
Note: SD= Standard Deviation, SEM= Standard Error of the Mean

Table A

	Test 1	Test 2	Test 3	Test 4	Test 5	Test 6	Test 7	Test 8	Test 9
1 (Dry)	26	25	24	22	25	32	32	35	30
CuN	16	18	23	20	27	25	26	30	25

Table B

Groups	Mean	SD	SEM
1 (Dry)	27.89	4.46	1.49
CuN	23.33	4.53	1.51

95% Confidence Interval

T-Value: 2.1512

Degrees of Freedom: 16

P-Value: 0.0471

B.2.8. Bacteriostatic vs Bactericidal

This test was performed in order to determine if the zones of inhibition present in the Kirby-Bauer tests against *S. mutans* were a result of bacteriostatic or bactericidal properties of the six tested MOF variations and copper (II) nitrate. From the zones of inhibition of each sample (Kirby-Bauer test), a swab was taken and then continuously streaked across an individual plate of Mueller-Hinton media. The plates were reviewed for the growth of *S. mutans* at 24 hours and 48 hours. The lack of growth would indicate that the *S. mutans* within the zones of inhibition had been killed and therefore the samples are bactericidal. The presence of growth would indicate that the samples had bacteriostatic properties and once removed from the presence of the samples, the *S. mutans* remained alive and capable of growing again.

Table 9. Bacteriostatic vs Bactericidal Tests. Seven samples were tested from the zones of inhibition from Kirby-Bauer tests, and after 48 hrs none of the plates with continuous streaking presented any growth of *S. mutans*, indicating the bacteria have been killed by the bactericidal properties of the samples.

Sample	Growth (24 Hrs)	Growth (48 Hrs)
1 Dry	None	None
1 EtOH wet	None	None
1 in mother solution	None	None
2 in mother solution	None	None
3 in mother solution	None	None
4 in mother solution	None	None
Copper (II) Nitrate	None	None
Control	Growth	Growth

B.2.9. Growth onto Titanium Implants

The MOFs' desired application relies on the growth of the frameworks directly onto titanium implants used in oral surgeries. To accomplish this goal, titanium implants were placed in the reaction vials prior to placement of the reaction solutions into the 85℃ oven for 24 hours. The MOFs were capable of growing directly onto the titanium implants (Figure 46). The attachment of the MOF crystals to the titanium substrate was confirmed through a series of washes with the mother solution and then ethanol, where none of the crystals were dislodged. The crystals were then scraped from the implants, and PXRD analysis was used to confirm that the production of the desired MOF was accomplished. Only a small amount of sample was able to be dislodged from the titanium implant, further indicating strong adherence to the metal surface, but the experimental peaks appear to correspond well with the expected calculated pattern. The absence of some peaks is likely due to the relatively small amount of sample, but no extra peaks are present also indicating pure phase 1.

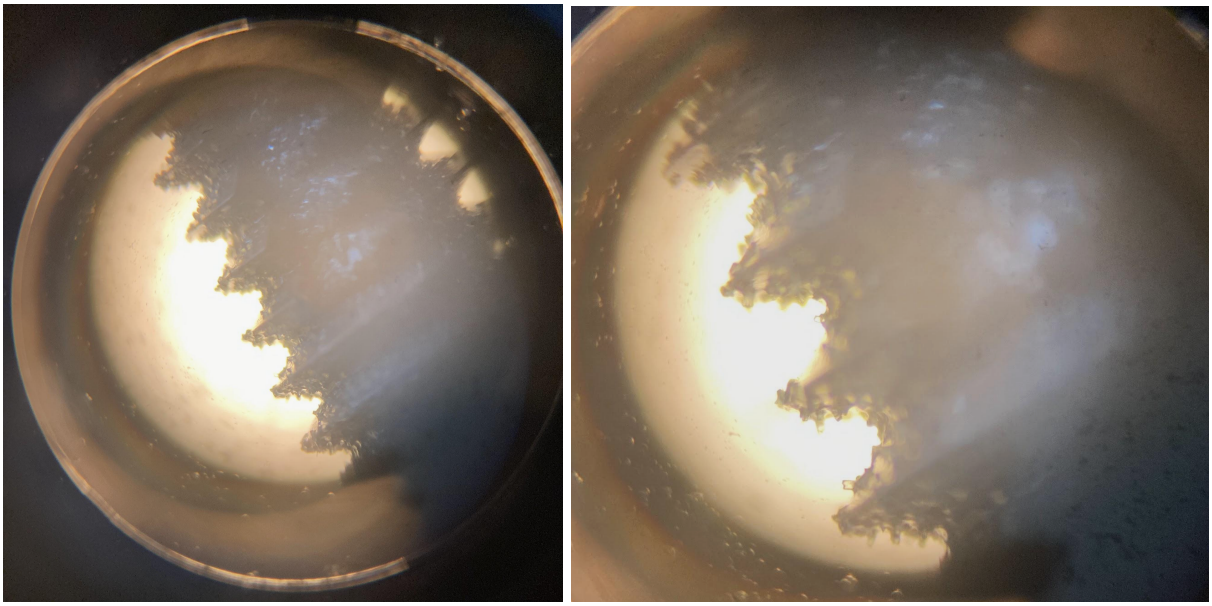

Figure 46: Microscopic Images of 1 onto a Titanium Implant (100x). Growth of **1** onto a titanium implant is present in this microscopic image.

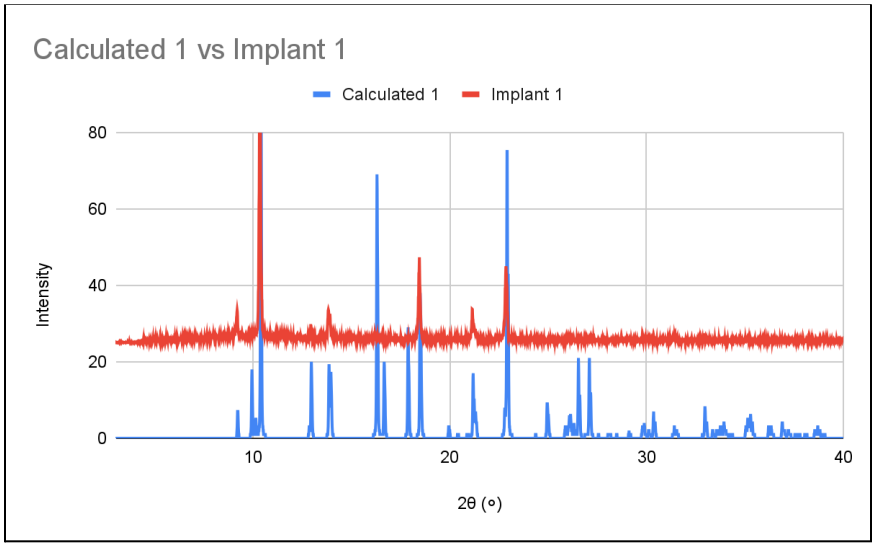

Figure 47: Calculated 1 vs Implant 1. As can be seen on the diffractogram, the peaks of implant **1** align well with calculated **1**, thus indicating that the crystals removed from the titanium implant are replicates of **1**. The peaks of implant **1** are low and limited due to the difficulty of removing crystals from the implant surface for PXRD analysis.

B.2.10. Sulfa-Drugs

Sulfa-drugs were tested for potential coordination in our MOF structures due to their known antimicrobial properties and potential for increased bacterial zones of inhibition. Pyridine was exchanged in the reaction conditions for sulfapyridine due to their similar molecular structures, which would increase the probability of sulfapyridine binding as a ligand. The resulting MOFs were powdery microcrystals so single crystal data could not be produced for the frameworks. Alternatively, IR spectroscopy was used for the identification of sulfapyridine's presence within the MOF structure. The MOFs were washed with mother solution to remove any excess reactants or potential contaminants, then EtOH was used as a low-boiling/volatile solvent to allow for more rapid/complete drying of the sample prior to running the IR spectroscopy.

Table 10: Reactions Conditions for the sulfapyridine phase.

Metal	Ligand	Solvents	Temperature
0.04mmol $Cu(NO_3)_2.2.5H_2O$	0.04mmol $H_2CDO{\cdot}1H_2O$	0.5mL DMF	40℃, 24hrs
		0.5mL EtOH	
		0.08 mmol sulfapyridine	

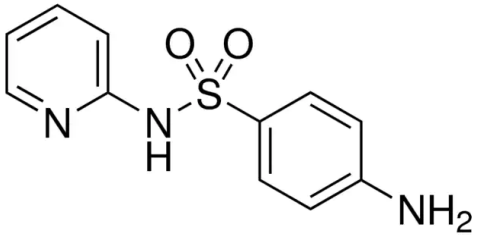

Figure 48: Molecular Structure of Sulfapyridine.[62]

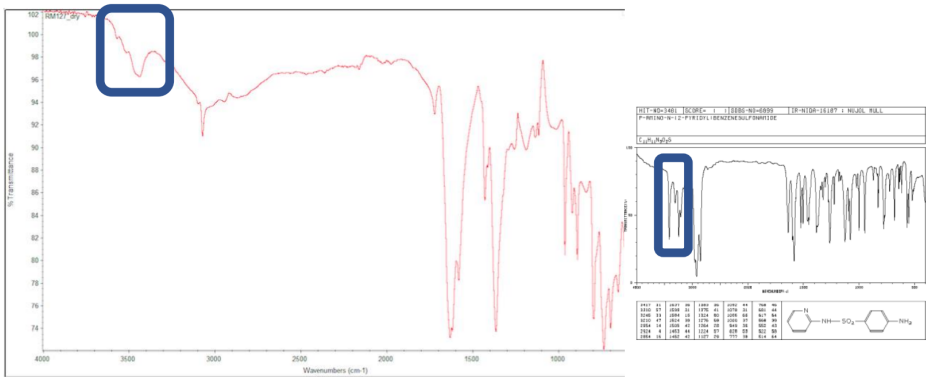

Figure 49: IR Spectra of the Sulfapyridine MOF Variant and Sulfapyridine.[63] The sulfapyridine MOF variant was prepared for IR spectroscopy through a series of ethanol washes prior to being dried. The circled regions above 3500cm^{-1} are indicative of amines. The presence of this peak in the MOF IR, although it has low intensity, indicates the presence of an amine in the framework. The "double fang" peaks around 1650cm^{-1} (C=O) and 1300cm^{-1} (C-O) are also important for consideration because the binding of a chelidonic acid in the structure would cause those peaks to shift closer to each other, as seen above.

C. Discussion

Through our preliminary research we have developed four main Cu-CDO MOF structures with varying terminal ligands. The variations in ligands were produced by adjusting the reactants and their concentrations until ideal conditions were determined for each desired structure (Figure 50). As can be seen in Figure 6, **1** consists of packed polymeric metal-organic (Cu-CDO) chains, having two pyridines and one water molecule as terminal ligands per trigonal bipyramidal metal ion. The neighboring chains interact through hydrogen bonds or pi-pi stacking. Reaction conditions were altered to provide a more anhydrous reaction environment (to avoid excess water, since **1** has a water ligand), resulting in **3**, structure shown in Figure 9. Interestingly, **3** consists of two different chains (Figure 12), causing the metal ions to have, essentially, 2.5 pyridines and 0.5 DMF terminal ligands, where a DMF or pyridine has replaced the would-be water ligand. Also, the coordination shifts slightly to more of a square pyramidal geometry. Although the pyridine ratio is much lower in solution, pyridine often binds Cu(II) much more efficiently/often than carbonyl O atoms (e.g., in DMF). The occurrence of both DMF or pyridine ligands in the axial position led us to explore the potential to target two new structures: 1) an "all DMF" structure, and 2) an "all pyridine" structure. In other words, could we replace half of the chains with more DMF terminal ligand or the other half with another pyridine? As expected, adding excess DMF, under anhydrous conditions, led to **2** (Figure 9) resulting in two pyridines and one DMF molecule as terminal ligands per metal ion, while the addition of excess pyridine led to **4**, with a pyridine for every terminal ligand, as can be seen in Figure 15. Thus, **3**'s structure results in a cross between **2** and **4** with one chain variant from each, and we were able to systematically design a series of unique Cu-CDO MOFs for antimicrobial testing.

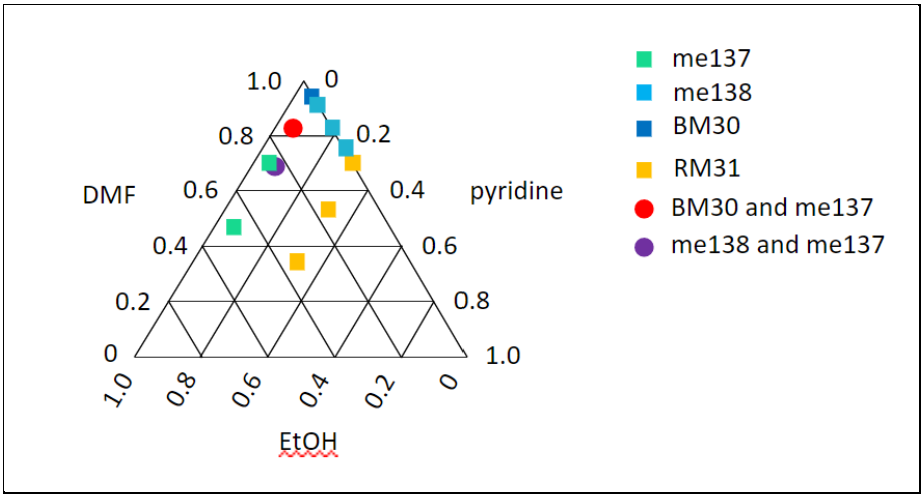

Figure 50: Solvent Ratio Variations. The scale is a ratio of 0.0 (0%) to 1.0 (100%); e.g., 0.5 is the ratio 0.5:0.5, and indicates 50%. Note: me137= **1**; BM30= **2**; me138= **3**; RM31= **4**

The first compound, $[Cu_2(CDO)_2(pyr.)_4(H_2O)_2]_n$ or phase **1**, was previously synthesized by Eubank et al. in 2007.[18] The reaction between $H_2CDO{\cdot}1H_2O$ and $Cu(NO_3)_2{\cdot}2.5H_2O$ in a dimethylformamide/ethanol/pyridine (DMF/EtOH/py) solution yields a homogeneous crystalline material. The identity and purity of **1** was confirmed by similarities between calculated and experimental PXRD (Figure 4). As can be seen in Figure 6, the metal-organic assembly (MOA) consists of a single type of Cu-chelidonate chain, which is composed of ditopic chelidonate (CDO) ligands bridging quasi trigonal bipyramidal single-copper ion units, $Cu(O_2CR)_2(py)_2(H_2O)$, where R indicates the CDO bridge and pyridine and water serve as terminal co-ligands. As such, each metal ion is coordinated to two nitrogen atoms and three oxygen atoms (CuN_2O_3). Each independent CDO is coordinated to two Cu(II) metal ions in a monodentate fashion through the carboxylates, thus serving as a dianionic bridging ligand and resulting in a neutral MOA.

The assembly of the alternating metal and organic moieties, both serving as bent secondary building units (SBUs), L-Cu-L (~132.181°) and Cu-L-Cu (~132.181°), results in the generation of zigzag metal-organic chains (Figure 6). The dicarboxylate angle in CDO is only ~115°, but the coordination of the most distal carboxylate O atoms leads to the wider Cu-L-Cu angle. In the crystal structure, neighboring zigzag chains interact along the x-axis through pi-pi stacking (Figure 6). Pairs of neighboring chains also interact along the y/z-axis through hydrogen bonding (HB), specifically O-H-O HBs, the importance of which will be discussed later. There are no uncoordinated molecules in the interstices.

In order to supplant the aquo ligand, we focused on the removal of potential sources of excess water from the synthesis conditions, including the use of anhydrous ligand and removal of EtOH (95%), leaving only DMF and pyridine with a large DMF excess. As expected, this led to the design and synthesis of phase **2**, $[Cu_2(CDO)_2(DMF)_2(pyr.)_4]_n$, where DMF replaces the water ligand. Although DMF coordination may be relatively less common compared to water or pyridine, for example, it is known in MOFs, including the archetypal MOF-5.[64]

The reaction between H_2CDO and $Cu(NO_3)_2 \cdot 2.5H_2O$ in a dimethylformamide/pyridine (DMF/py) solution yields a homogeneous macrocrystalline material. The identity and purity of **2** was confirmed by similarities between calculated and experimental (PXRD) (Figure 7). As can be seen in Figure 9, the MOA consists of a single type of Cu-chelidonate chain, which is composed of ditopic chelidonate (CDO) ligands bridging quasi square bipyramidal single-copper ion units, $Cu(O_2CR)_2(py)_2(H_2O)$, where R indicates the CDO bridge and pyridine and DMF serve as terminal co-ligands. As such, each metal ion is coordinated to two nitrogen atoms and three oxygen atoms (CuN_2O_3). Each independent CDO is coordinated to two Cu(II) metal ions in a monodentate fashion through the carboxylates, thus serving as a dianionic bridging ligand and resulting in a neutral MOA.

Here the geometry shifts slightly to quasi square pyramidal Cu(II), CuN_2O_3, which introduces a pseudo linear metal building unit (CuO_2, ~167°$_{\text{avg O-Cu-O}}$), but the bent angle of CDO (~102.335°) still produces zigzag chains (Figure 9). The dicarboxylate angle in CDO is only ~115°, but the coordination of the most distal carboxylate O atoms leads to the wider Cu-L-Cu angle. In the crystal structure, neighboring zigzag chains interact along the y axis through pi-pi stacking (Figure 9). Pairs of neighboring chains also interact along the x-axis through hydrogen bonding (HB), specifically O-H-O HBs. There are no uncoordinated molecules in the interstices.

We theorized that the conversion rate could be controlled by modifying the amount or identity of the co-ligand present in the structure. By utilizing a mixed-solvent system with a lower DMF:pyr. ratio, we were able to synthesize a unique intermediate MOA, phase **3** $\{[Cu_2(CDO)_2(DMF)(pyr.)_5]_n\}$ with a combination of two types of metal-organic chains or $[Cu(CDO)(py)_2(DMF)\text{-}Cu(CDO)(py)_3]_n$. The reaction between H_2CDO and $Cu(NO_3)_2 \cdot 2.5H_2O$ in a reduced dimethylformamide and constant pyridine (DMF/py) solution, in comparison with **2**, yields a homogeneous crystalline material. The identity and purity of **3** was confirmed by similarities between calculated and experimental PXRD (Figure 10).

As can be seen in Figure 12, the MOA consists of two types of Cu-chelidonate chain, with a mix between a pure DMF (axial) and py (axial) structure. One chain is identical to those found in **2**, and the other has only py terminal co-ligands. For both chain variations, the ligands are bridging quasi square bipyramidal single-copper ion units, $Cu(O_2CR)_2(py)_2(H_2O)$, where R indicates the CDO bridge and pyridine or DMF, depending on the chain, serve as terminal co-ligands. As such, each metal ion is coordinated to a combination of either two nitrogen atoms and three oxygen atoms (CuN_2O_3) or three nitrogen atoms and two oxygen atoms (CuN_3O_2). Each independent CDO is coordinated to two Cu(II) metal ions in a monodentate fashion through the carboxylates, thus serving as a dianionic bridging ligand and resulting in a neutral MOA.

The axial pyridine bond with Cu ($Cu\text{-}N_{py(ax)}$, ~2.227 Å) in **3** is longer than the comparable bond with DMF ($Cu\text{-}O_{DMF(ax)}$, ~2.274 Å) in **3** (and **2**). This supported a stronger coordinate bond with pyridine and suggested that the material would better resist conversion to **1**. As predicted, successive PXRD runs indicate that **3** takes ~72 mins to fully convert to **1** (Table 5).

Upon seeing the second type of chain with all pyr. terminal co-ligands, we theorized that the addition of excess py to the synthesis conditions would lead to a fourth phase consisting of only one type of py-based chain. As expected, the reaction between H_2CDO and $Cu(NO_3)_2{\cdot}2.5H_2O$ in a dimethylformamide and excess pyridine (DMF/py) solution, above 0.8 mL, led to the targeted material **4** $\{[Cu_2(CDO)_2(pyr.)_6]_n\}$. The reaction yields a homogeneous crystalline material with metal-organic chains that are identical to the py-based chains found in **3**. The identity and purity of **4** was confirmed by similarities between calculated and experimental PXRD (Figure 13).

As can be seen in Figure 15, the MOA consists of a single type of Cu-chelidonate chain, which is composed of ditopic chelidonate (CDO) ligands bridging quasi trigonal bipyramidal single-copper ion units, $Cu(O_2CR)_2(py)_2(H_2O)$, where R indicates the CDO bridge and pyridine serves as a terminal co-ligand. The axial pyridine bond with Cu ($Cu\text{-}N_{py(ax)}$) in **4** is longer than the comparable bond with DMF ($Cu\text{-}O_{DMF(ax)}$) in **2** and **3.** Each metal ion is coordinated to two nitrogen atoms and three oxygen atoms (CuN_2O_3). Each independent CDO is coordinated to two Cu(II) metal ions in a monodentate fashion through the carboxylates, thus serving as a dianionic bridging ligand and resulting in a neutral MOA.

Through single crystal data analysis, a set of PXRD calculated values were produced for each of our novel MOFs. We then used those calculated values for comparison against our

experimental PXRD values and confirmation of our structure. The reproducibility and purity of each framework structure is crucial to the study and use of these materials for applications. Consistency in conditions and results had to be obtained so each set of frameworks had an experimental PXRD for comparison to the calculated values. The comparisons between an experiment PXRD of each MOF structure and their calculated values can be seen in Figures 4, 7, 10, and 13, respectively. Also, in the presence of relatively high ambient humidity the MOF structures experienced conversions, which are related to stability and ligand associations.

There was a high tendency for MOF phases 2-4 to convert to **1** through exposure to relatively high ambient humidity, and the comparisons between PXRD experimental values and the calculated values could be used to track those transitions. During a PXRD scan, there was a noticeable color change in the **3** crystals on the plate. A second PXRD was run shortly after and the diffractogram had changed to express peaks indicative of **1**. By placing the crystals of **2**-**4** into varying environments it was determined that neither x-rays nor ambient light were the cause of the transitions. It was noted that **1** is the only structure with coordinated water, and we theorized that due to the high relative humidity in the laboratory environment, **2**-**4** absorbed moisture to convert to **1**. The transitions expressed through a series of PXRD scans indicate that the frameworks are converting to a more stable structure. The stability of the MOF structures is heavily related to their efficacy for dental applications. The MOFs that we are producing will be placed in highly aqueous environments with high humidity when attached to implants for oral surgery, so it was vital to determine the effects on stability under those conditions. Tests for each MOF structure were run at ambient temperature (20- 21.67℃) and when the humidity was between 58-63% so that the structures could be exposed to an environment with relatively high humidity. Structures **2**, **3**, and **4** all appear to have converted to **1** in the presence of humidity at predicted systematic rates (Table 5). The conversion was supported by and tracked using PXRD experimental values in comparison with the single-crystal calculated PXRD pattern. **2**'s conversion can be tracked between Figure 21- 24, while compared visually between Figure 20 and Figure 24. **3**'s conversion can be tracked between Figure 26 and Figure 28, while compared visually between Figure 25 and 27. **4**'s conversion can be tracked between Figure 30 and 32, while compared visually between Figure 29 and Figure 31. The conversion of **2** (having more of the labile DMF ligands) occurred at the fastest rate of 62 minutes (Figure 33). Followed by **3** at 72 minutes and then **4** at 82 minutes (Table 5). The water molecule terminal ligands in **1** allow for hydrogen bonding between chains, while none of our other structures have the water

molecule terminal ligands for similar bonding (Figure 51). The stronger interactions between **1**'s molecular structure allows for it to be the most stable framework in environments with humidity.[65] **1** is the favored MOF structure under high humidity and has the ability to maintain its structure for several hours when placed directly in DI water, as seen in the PXRDs of Figure 37. These results provided us with the confidence that **1** was best suited for placement in an aqueous, biological environment such as the oral cavity if a stable framework is desired.

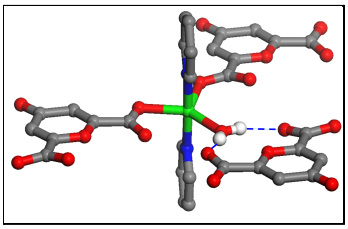

Figure 51. Hydrogen bonding in **1** vs the relaxed structure of **1**, obtained from computational data: a) A portion of **1** from the crystal structure showing its inherent interchain OH_O hydrogen bonds; b) a portion of **1** from the crystal structure showing the chain structure; c) a portion of **1** from the crystal structure showing its inherent interchain OH_O hydrogen bonds.

Similar to the effects of humidity on MOFs **2-4,** if any of our main four MOF structures were left exposed to UV light for extended periods of time then new peaks would begin to develop on the PXRD data while others decrease or disappear (Figure 38). This indicates that prolonged exposure to UV light has an effect on the stability and structure of our frameworks. The conversion under UV light leads to considerations in the preparation, storage, and potential applications of our MOFs. The altered framework produced after UV exposure has the potential to act as a more stable structure than any of our four main MOFs, which could provide benefits in the applications of our frameworks, such as controlled degradation. UV light is also commonly used with the preparation and placement of sealants and fillings so if the UV-altered framework is desired then the dental light could be used for MOF activation as the dental procedure or surgery is taking place.

Once an understanding of the stability and environmental interactions of the MOFs were established, the research focus shifted to their potential for bacterial inhibition. Through Kirby-Bauer testing we analyzed our framework's antimicrobial properties, as well as, their individual components against *S. mutans*. The reaction components were tested to discover if our frameworks had a synergistic effect and could produce a combined zone of inhibition greater

than all of the materials independently. All of our MOFs had average zones of inhibition at least 2.5mm larger than the largest individual component zone of inhibition, which was produced by copper (II) nitrate (Table 7). The next largest individual component, H_2CDO, averaged 8.75mm smaller than the smallest MOF zone of inhibition. In order to determine statistical significance, the smallest MOF zone of inhibition, from **1** dry, was compared against the largest individual component zone of inhibition, from copper (II) nitrate. Nine Kirby-Bauer tests were run for both compounds for increased certainty in the statistical significance of our T-test results. The nine zone-of-inhibition values of **1** dry (M= 27.89, SD= 4.46) compared to the nine zone-of-inhibition values of copper (II) nitrate (M= 23.33, SD= 4.53) demonstrated that **1** dry had significantly larger zones of inhibition, $t(16)= 2.1512$, $p= 0.0471$ (Table 8A & 8B). Since the MOF variant with the smallest zone of inhibition was larger than the greatest individual component's, it can be confirmed that all MOFs have zones of inhibition that are greater than any of their individual components by a statistically significant amount. These findings help affirm that our goal of a synergistic antimicrobial effect in our MOFs was obtained.

A very significant component of the use of our MOFs towards the larger goal of preventing peri-implantitis is the ability for our frameworks to prevent the growth of oral bacteria such as *S. mutans*. Kirby-Bauer tests are often used for the determination of the efficacy of a known antimicrobial compound against known bacterial variants. However, the MOFs developed in our study are either novel or too recently published to have a standardized series of ranges for if *S. mutans* is resistant, intermediate, or susceptible to them. Instead, a comparison must be made between the ranges for the current antimicrobial standard of care and the average zones of inhibition for our MOFs. In a research article published in 2020 the most commonly prescribed antimicrobial rates post oral surgery were defined as the following; penicillin (45.25%), penicillin with beta-lactamase inhibitors (18.76%), metronidazole (12.29%), and second-to-fourth generation cephalosporins (11.52%).[13] By using a diffusion zone diameter chart to find the standard inhibition zone ranges, the four most common antimicrobials can be averaged with their perspective rate proportions to produce the ranges; resistant- less than or equal to 22.35mm, intermediate- 22.35mm to 27.67mm, susceptible- greater or equal to 27.67mm .[66,67] By these standards, all of our MOFs are considered to be quite effective antimicrobials due to their averages being within the highest range, the susceptible range (Table 7). This result indicates that the tested concentration of our antimicrobial agent is effective against *S. mutans* and could be used to treat an infection by that bacteria. However, all individual

components of our MOFs fell within the resistant or intermediate range. These ranges indicate that the components are either unreliable antimicrobial agents or higher concentrations could potentially be effective against *S. mutans*. As concentrations increase it is important to consider toxicity within a biological system, so our MOFs have the added benefit of not needing a higher concentration, thus increasing their biocompatibility in comparison to their individual components.

Also, due to the versatility of MOF structures, we explored synthesizing analogous MOFs with zinc ions. Zinc nitrate was tested under reaction conditions similar to **1** (Table 6), and we were able to produce the Zn-CDO analog. The zinc metal ions, which are known to have higher biocompatibility than copper, have also produced MOFs with antimicrobial properties and hold the potential for an even more biocompatible variation of the four main MOF structures in this study (Figure 43).

In a majority of instances, bactericidal antimicrobials are preferred over bacteriostatic due to their ability to kill the targeted bacteria and prevent continued or recurrent infections.[7] Bacteriostatic antimicrobials prevent the growth of bacteria and prevent them from replicating, but do not fully kill the microbes. If the bacteriostatic agents are removed then the bacteria are capable of replicating again, which results in recurring infections that appear to be eliminated.

Thus, once it was found that the MOFs were effective antimicrobials against *S. mutans*, the bacteriostatic or bactericidal method of inhibition was researched to determine the function of the inhibition. As described above, the *S. mutans* removed from the zones of inhibition of the MOFs and copper (II) nitrate did not begin to replicate again after 48 hours, while the control sample with no MOF present did exhibit growth (Table 9). Our testing method provides evidence indicative of our MOFs functioning in the preferred bactericidal nature. However, it is important to note that our methods for testing bacteriostatic versus bactericidal methods of inhibition are reasonably simple due to the materials at our disposal and the focus of the research project. More reliable means of determining the function of bacterial inhibition are available through dilutions, cytometry, and growth curve studies.[68–70]

The intended use for the MOFs developed in this study is to grow them directly onto implants used in oral surgeries so that a zone of inhibition is present as the implant is placed and for an extended period of time post-surgery. MOF growth tests were performed with titanium implants, the most common oral implant, that were provided by a local oral surgeon. As can be seen in Figure 46, the growth tests were a success (i.e., crystals are evident on the surface) and

after washing with the mother solution and ethanol the crystals remained intact on the implant. Through PXRD scans of crystals removed from the titanium implant and comparison to calculated PXRDs from single-crystal data, we were able to determine that the desired MOFs had been produced on the Ti surface (Figure 47). If the size of the crystals needs to be modified in order to preserve the function and ease of placement of the implant, then our reaction conditions could easily be altered to produce smaller particles or even thin films, further evidence of the versatility of MOFs.

One of the methods tested for the production of microcrystals and thin-film MOFs includes varying the reaction solvent to DMSO, DBF, or DEF for **1**. An excess of DMF as the solvent also produces microcrystals and often thin films for all four main MOF conditions. It was also found that the addition of sulfapyridine in the place of pyridine in the reaction conditions with a decrease in reaction temperature, would produce microcrystals and thin films while incorporating the sulfa-drug. The thin film will allow for maintained implant function, while also providing the desired antimicrobial properties to the site of the oral surgery. A mechanical filing method could also be used to smooth the MOF material to be more homogenous on the Ti surface.

Preliminary testing of sulfapyridine as a terminal ligand in our MOF structures was conducted, and through IR spectroscopy the sulfa-drug could be identified within the framework. After removing all uncoordinated sulfapyridine molecules with a mother solution and then ethanol wash, IR was run over the dry MOF and peaks were present in the range above 3500cm^{-1} (Figure 49). The peaks within this range are indicative of the N-H stretch in primary and secondary amines and the presence of a multiplet allows for the assumption that sulfapyridine is present within the framework structure. The “double fang” peaks around 1650cm^{-1} (C=O) and 1300cm^{-1} (C-O) are also important for consideration because the binding of chelidonic acid in the structure would cause those peaks to shift closer to each other, as seen in Figure 49. Despite the coordination of sulfapyridine into a MOF structure, reaction conditions could not be identified to produce suitable single crystals for analysis. We have determined that sulfapyridine-MOF production reactions need to be held at lower temperatures than MOFs with pyridine terminal ligands or degradation of the materials will occur before a crystalline MOF structure can be produced. The initial progress of producing a sulfapyridine-MOF variant provides promising results for the coordination of such a drug molecule directly into a framework and a foundation for future studies.

D. Conclusion

A series of metal-organic frameworks were systematically developed and their properties analyzed for the potential of preventing peri-implantitis from *S. mutans* post oral surgery. The initial focus was on reproducing frameworks or developing novel MOFs so that frameworks with a high potential for antimicrobial inhibition could be identified for further research in the study. Four key MOFs were identified, all containing bridging chelidonate ligands and copper (II) metal ions, but with variations of the terminal ligands on their structures. **1** has a MBB with two pyridine terminal ligands and one water molecule terminal ligands per metal ion (Figure 6). Hydrogen bonding is a strong horizontal coordination between the chains of **1**, which allows for a more stable structure in comparison to the other three main MOFs. **2**'s MBB contains two pyridines and one DMF terminal ligand per metal ion (Figure 9). **3** is composed of two chain variants, one with the same terminal ligand bonding as **2** and the other with all pyridine terminal ligands, the same as **4** (Figures 12 & 15). All frameworks consist of pi-pi stacking between neighboring chains. Once the frameworks were developed and identified, their stability and ability to interact with a biological environment were studied.

Humidity, full submersion in DI water, and UV exposure were all analyzed for effects on structural composition and the potential for directed or delayed antimicrobial delivery. **2**, **3**, and **4** all experienced molecular changes when exposed to humidity within the environment, and the end product of their conversion was identical to the framework of **1**. The conversion of **2** occurred at the fastest rate of 62 minutes (Figure 33). Followed by **3** at 72 minutes and then **4** at 82 minutes (Table 5). The delayed degradation of the three frameworks in response to humidity provides the potential for their structures to be used as carriers of antimicrobial compounds for directed/controlled release applications. The humidity-stable phase, **1**, was then tested for further stability once submerged directly within DI water. The structure of **1** was maintained for several hours (approximately 24hrs), providing confidence that this framework variant could be used as a time-stable phase within biological settings. After extended exposure to UV light, full conversion of all four frameworks to a potentially more stable UV phase was determined (Figure 38). With the common practice of high strength, UV-curing of fillings and sealants, the UV phase could also be used for controlled delivery of antimicrobial properties.

Following the analysis of our MOFs' properties under varying conditions, Kirby-Bauer testing was used to determine their antimicrobial abilities. It was determined that all frameworks

produced zones of inhibition that were larger than any individual component by a statistically significant amount (Table 8). These results indicate that the combination of MOF ligands and copper metal ions produced the desired synergistic antimicrobial effect greater than any individual component. The level of bacterial inhibition was also estimated using the Kirby-Bauer tests by proportionally averaging the standard inhibition zone ranges of the four most common antimicrobials for reference. All of our MOFs were considered to be effective antimicrobials due to their averages being within the calculated susceptible ranges of the averaged oral surgery antimicrobials (Table 7). This result indicates that the tested concentration of our MOFs is effective against *S. mutans* and is capable of treating an infection by it. In order to determine the function by which the frameworks were inhibiting bacterial growth a preliminary bacteriostatic versus bactericidal test was performed. It was found that all MOFs were bactericidal, which provides the added benefit of killing the *S. mutans* within the zone of inhibition entirely and preventing recurrent infections in the biological setting.

For the intended application of our MOFs, they needed to have the capability of direct growth onto oral surgery implants. This function was tested through the placement of oral surgery implants made of the most common material, titanium, into the reaction conditions of our frameworks. Growth onto the implants was successful and large crystals were clearly adhered to the titanium surface, including after washing processes. Through the variation of reaction conditions, microcrystals could be produced onto the implant, which has the added benefit of a reduced impact on the function of the implant within the surgery. If needed, mechanical abrasion could also be used to file the larger frameworks into a smooth surface if needed. The ability for our now-proven, statistically-significant, synergistically antimicrobial MOFs to grow directly onto titanium implants allows them to be present as the implant is being placed, thus producing a lasting zone of inhibition before, and long after, the surgery is completed.

Preliminary testing of sulfa-drugs was conducted but we were unable to find the proper reaction conditions for producing crystals large enough to be used in the single-crystal x-ray diffractometer. Microcrystals were produced with sulfapyridine incorporated into the framework, as indicated by the corresponding peaks present in the IR spectra. Future testing of reaction conditions could provide large enough crystals for analysis and then their applications as potentially stronger antimicrobials than any of the four main MOFs in this study. The addition of sulfapyridine into our MOF frameworks increases the potential synergistic antimicrobial

properties and could be beneficial for directed drug delivery. Preliminary data was also produced through our methods of bacteriostatic versus bactericidal tests, but further, in-depth, studies would be needed for the confirmation of the results. More reliable means of determining the function of bacterial inhibition are available through dilutions, cytometry, and growth curve studies. In addition to further research on the areas of preliminary data within this project, the area of greatest interest for future studies lies in *in vivo* studies. All analyses and tests performed by our group were limited to *in vitro* environments, but the culmination of our results provides confidence in the function of the four key MOFs. Although rigorous regulations and certifications must be met prior to *in vivo* studies, the true efficacy of our frameworks in biological environments can only be determined by these forms of research. The antimicrobial properties of our MOFs against *S. mutans*, their delayed or directed application through stability variations, and their ability to be grown directly onto titanium implants provides them with all desired properties for the prevention of peri-implantitis post oral surgery.

E. References Cited

(1) Moy, P. K.; Medina, D.; Shetty, V.; Aghaloo, T. L. Dental Implant Failure Rates and Associated Risk Factors. *Int. J. Oral Maxillofac. Implants* **2005**, *20* (4), 569–577.

(2) Wittneben, J.-G.; Buser, D.; Salvi, G. E.; Bürgin, W.; Hicklin, S.; Brägger, U. Complication and Failure Rates with Implant-Supported Fixed Dental Prostheses and Single Crowns: A 10-Year Retrospective Study. *Clin. Implant Dent. Relat. Res.* **2014**, *16* (3), 356–364. https://doi.org/10.1111/cid.12066.

(3) Geremias, T. C.; Montero, J. F. D.; Magini, R. de S.; Schuldt Filho, G.; de Magalhães, E. B.; Bianchini, M. A. Biofilm Analysis of Retrieved Dental Implants after Different Peri-Implantitis Treatments. *Case Rep. Dent.* **2017**, *2017*, e8562050. https://doi.org/10.1155/2017/8562050.

(4) Gangu, K. K.; Maddila, S.; Mukkamala, S. B.; Jonnalagadda, S. B. A Review on Contemporary Metal–Organic Framework Materials. *Inorganica Chim. Acta* **2016**, *446*, 61–74. https://doi.org/10.1016/j.ica.2016.02.062.

(5) Pettinari, C.; Pettinari, R.; Di Nicola, C.; Tombesi, A.; Scuri, S.; Marchetti, F. Antimicrobial MOFs. *Coord. Chem. Rev.* **2021**, *446*, 214121. https://doi.org/10.1016/j.ccr.2021.214121.

(6) Wang, M.; Zhou, X.; Li, Y.; Dong, Y.; Meng, J.; Zhang, S.; Xia, L.; He, Z.; Ren, L.; Chen, Z.; Zhang, X. Triple-Synergistic MOF-Nanozyme for Efficient Antibacterial Treatment. *Bioact. Mater.* **2022**, *17*, 289–299. https://doi.org/10.1016/j.bioactmat.2022.01.036.

(7) Bétard, A.; Fischer, R. A. Metal–Organic Framework Thin Films: From Fundamentals to Applications. *Chem. Rev.* **2012**, *112* (2), 1055–1083. https://doi.org/10.1021/cr200167v.

(8) Pankey, G. A.; Sabath, L. D. Clinical Relevance of Bacteriostatic versus Bactericidal Mechanisms of Action in the Treatment of Gram-Positive Bacterial Infections. *Clin. Infect. Dis.* **2004**, *38* (6), 864–870. https://doi.org/10.1086/381972.

(9) Pinto, R. V.; Wang, S.; Tavares, S. R.; Pires, J.; Antunes, F.; Vimont, A.; Clet, G.; Daturi, M.; Maurin, G.; Serre, C.; Pinto, M. L. Tuning Cellular Biological Functions Through the Controlled Release of NO from a Porous Ti-MOF. *Angew. Chem. Int. Ed.* **2020**, *59* (13), 5135–5143. https://doi.org/10.1002/anie.201913135.

(10) Jaw (Orthognathic) Anatomy and Problems, Understanding https://mountnittany.org/wellness-article/jaw-orthognathic-anatomy-and-problems-understanding (accessed 2022 -03 -27).

(11) Oral Surgical Procedures | FAQs | Infection Control | Division of Oral Health | CDC https://www.cdc.gov/oralhealth/infectioncontrol/faqs/oral-surgical-procedures.html (accessed 2022 -03 -29).

(12) Suda, K. J.; Henschel, H.; Patel, U.; Fitzpatrick, M. A.; Evans, C. T. Use of Antibiotic Prophylaxis for Tooth Extractions, Dental Implants, and Periodontal Surgical Procedures. *Open Forum Infect. Dis.* **2017**, *5* (1), ofx250. https://doi.org/10.1093/ofid/ofx250.

(13) Choi, Y.-Y. Prescription of Antibiotics after Tooth Extraction in Adults: A Nationwide Study in Korea. *J. Korean Assoc. Oral Maxillofac. Surg.* **2020**, *46* (1), 49–57. https://doi.org/10.5125/jkaoms.2020.46.1.49.

(14) Tibbetts, I.; Kostakis, G. E. Recent Bio-Advances in Metal-Organic Frameworks. *Mol. Basel Switz.* **2020**, *25* (6). https://doi.org/10.3390/molecules25061291.

(15) Sun, Y.; Zheng, L.; Yang, Y.; Qian, X.; Fu, T.; Li, X.; Yang, Z.; Yan, H.; Cui, C.; Tan, W. Metal–Organic Framework Nanocarriers for Drug Delivery in Biomedical Applications. *Nano-Micro Lett.* **2020**, *12* (1), 103. https://doi.org/10.1007/s40820-020-00423-3.

(16) Safy, M. E. A.; Amin, M.; Haikal, R. R.; Elshazly, B.; Wang, J.; Wang, Y.; Wöll, C.; Alkordi, M. H. Probing the Water Stability Limits and Degradation Pathways of Metal–Organic Frameworks. *Chem. – Eur. J.* **2020**, *26* (31), 7109–7117. https://doi.org/10.1002/chem.202000207.

(17) Schoenecker, P. M.; Carson, C. G.; Jasuja, H.; Flemming, C. J. J.; Walton, K. S. Effect of Water Adsorption on Retention of Structure and Surface Area of Metal–Organic

Frameworks. *Ind. Amp Eng. Chem. Res. 51* (18), 6513–6519.
(18) Eubank, J.; Kravtsov, V.; Eddaoudi, M. Synthesis of Organic Photodimeric Cage Molecules Based on Cycloaddition via Metal− Ligand Directed Assembly. *J. Am. Chem. Soc.* **2007**, *129* (18), 5820–5821.
(19) Shang, J.; Chai, M.; Zhu, Y. Photocatalytic Degradation of Polystyrene Plastic under Fluorescent Light. *Environ. Sci. Technol.* **2003**, *37* (19), 4494–4499. https://doi.org/10.1021/es0209464.
(20) Kawabata, K.; Sugihara, K.; Sanoh, S.; Kitamura, S.; Ohta, S. Photodegradation of Pharmaceuticals in the Aquatic Environment by Sunlight and UV-A, -B and -C Irradiation. *J. Toxicol. Sci.* **2013**, *38* (2), 215–223. https://doi.org/10.2131/jts.38.215.
(21) Grass, G.; Rensing, C.; Solioz, M. Metallic Copper as an Antimicrobial Surface. *Appl. Environ. Microbiol.* **2011**, *77* (5), 1541–1547. https://doi.org/10.1128/AEM.02766-10.
(22) Kirkwood, Z. I.; Millar, B. C.; Downey, D. G.; Moore, J. E. Antimicrobial Effect of Dimethyl Sulfoxide and N, N-Dimethylformamide on Mycobacterium Abscessus: Implications for Antimicrobial Susceptibility Testing. *Int. J. Mycobacteriology* **2018**, *7* (2), 134–136. https://doi.org/10.4103/ijmy.ijmy_35_18.
(23) El-Sayed, H. A.; Moustafa, A. H.; El-Torky, A. E.; Abd El-Salam, E. A. A Series of Pyridines and Pyridine Based Sulfa-Drugs as Antimicrobial Agents: Design, Synthesis and Antimicrobial Activity. *Russ. J. Gen. Chem.* **2017**, *87* (10), 2401–2408. https://doi.org/10.1134/S107036321710022X.
(24) Alkordi, M. H.; Belof, J. L.; Rivera, E.; Wojtas, L.; Eddaoudi, M. Insight into the Construction of Metal–Organic Polyhedra: Metal–Organic Cubes as a Case Study. *Chem. Sci.* **2011**, *2* (9), 1695–1705. https://doi.org/10.1039/C1SC00269D.
(25) Lee, D. T.; Zhao, J.; Oldham, C. J.; Peterson, G. W.; Parsons, G. N. UiO-66-NH2 Metal–Organic Framework (MOF) Nucleation on TiO2, ZnO, and Al2O3 Atomic Layer Deposition-Treated Polymer Fibers: Role of Metal Oxide on MOF Growth and Catalytic Hydrolysis of Chemical Warfare Agent Simulants. *ACS Appl. Mater. Interfaces* **2017**, *9* (51), 44847–44855. https://doi.org/10.1021/acsami.7b15397.
(26) Li, J.; Wang, L.; Liu, Y.; Song, Y.; Zeng, P.; Zhang, Y. The Research Trends of Metal-Organic Frameworks in Environmental Science: A Review Based on Bibliometric Analysis. *Environ. Sci. Pollut. Res.* **2020**, *27* (16), 19265–19284. https://doi.org/10.1007/s11356-020-08241-1.
(27) Lei, J.; Qian, R.; Ling, P.; Cui, L.; Ju, H. Design and Sensing Applications of Metal–Organic Framework Composites. *TrAC Trends Anal. Chem.* **2014**, *58*, 71–78. https://doi.org/10.1016/j.trac.2014.02.012.
(28) Keskin, S.; Kızılel, S. Biomedical Applications of Metal Organic Frameworks. *Ind. Eng. Chem. Res.* **2011**, *50* (4), 1799–1812. https://doi.org/10.1021/ie101312k.
(29) Yang, Y.; Aloysius, H.; Inoyama, D.; Chen, Y.; Hu, L. Enzyme-Mediated Hydrolytic Activation of Prodrugs. *Acta Pharm. Sin. B* **2011**, *1* (3), 143–159. https://doi.org/10.1016/j.apsb.2011.08.001.
(30) Chung, Y. G.; Haldoupis, E.; Bucior, B. J.; Haranczyk, M.; Lee, S.; Zhang, H.; Vogiatzis, K. D.; Milisavljevic, M.; Ling, S.; Camp, J. S.; Slater, B.; Siepmann, J. I.; Sholl, D. S.; Snurr, R. Q. Advances, Updates, and Analytics for the Computation-Ready, Experimental Metal–Organic Framework Database: CoRE MOF 2019. *J. Chem. Eng. Data* **2019**, *64* (12), 5985–5998. https://doi.org/10.1021/acs.jced.9b00835.
(31) Kökçam-Demir, Ü.; Goldman, A.; Esrafili, L.; Gharib, M.; Morsali, A.; Weingart, O.; Janiak, C. Coordinatively Unsaturated Metal Sites (Open Metal Sites) in Metal–Organic Frameworks: Design and Applications. *Chem. Soc. Rev.* **2020**, *49* (9), 2751–2798. https://doi.org/10.1039/C9CS00609E.
(32) Febré, N.; Silva, V.; Báez, A.; Palza, H.; Delgado, K.; Aburto, I.; Silva, V. [Antibacterial activity of copper salts against microorganisms isolated from chronic infected wounds]. *Rev. Med. Chil.* **2016**, *144* (12), 1523–1530.

https://doi.org/10.4067/S0034-98872016001200003.
(33) Shimabukuro, M. Antibacterial Property and Biocompatibility of Silver, Copper, and Zinc in Titanium Dioxide Layers Incorporated by One-Step Micro-Arc Oxidation: A Review. *Antibiot. Basel Switz.* **2020**, *9* (10). https://doi.org/10.3390/antibiotics9100716.
(34) Lesch, J. E. *The First Miracle Drugs: How the Sulfa Drugs Transformed Medicine*; Oxford University Press, 2007.
(35) Goodall, R. E. Sulfonamide Drugs as an Adjunct in Handling Dental Infections. *J. Am. Dent. Assoc.* **1944**, *31* (11), 752–758. https://doi.org/10.14219/jada.archive.1944.0177.
(36) Poveda Roda, R.; Bagan, J. V.; Sanchis Bielsa, J. M.; Carbonell Pastor, E. Antibiotic Use in Dental Practice. A Review. *Med. Oral Patol. Oral Cirugia Bucal* **2007**, *12* (3), E186-192.
(37) Koszelewski, D.; Ostaszewski, R.; Śmigielski, P.; Hrunyk, A.; Kramkowski, K.; Laskowski, Ł.; Laskowska, M.; Lizut, R.; Szymczak, M.; Michalski, J.; Gawin, K.; Kowalczyk, P. Pyridine Derivatives—A New Class of Compounds That Are Toxic to E. Coli K12, R2–R4 Strains. *Materials* **2021**, *14* (18), 5401. https://doi.org/10.3390/ma14185401.
(38) Volin, M. V.; Harlow, L. A.; Woods, J. M.; Campbell, P. L.; Amin, M. A.; Tokuhira, M.; Koch, A. E. Treatment with Sulfasalazine or Sulfapyridine, but Not 5-Aminosalicyclic Acid, Inhibits Basic Fibroblast Growth Factor-Induced Endothelial Cell Chemotaxis. *Arthritis Rheum.* **1999**, *42* (9), 1927–1935. https://doi.org/10.1002/1529-0131(199909)42:9<1927::AID-ANR19>3.0.CO;2-X.
(39) Hoop, M.; Walde, C. F.; Riccò, R.; Mushtaq, F.; Terzopoulou, A.; Chen, X.-Z.; deMello, A. J.; Doonan, C. J.; Falcaro, P.; Nelson, B. J.; Puigmartí-Luis, J.; Pané, S. Biocompatibility Characteristics of the Metal Organic Framework ZIF-8 for Therapeutical Applications. *Appl. Mater. Today* **2018**, *11*, 13–21. https://doi.org/10.1016/j.apmt.2017.12.014.
(40) Lin, W.; Cui, Y.; Yang, Y.; Hu, Q.; Qian, G. A Biocompatible Metal–Organic Framework as a PH and Temperature Dual-Responsive Drug Carrier. *Dalton Trans.* **2018**, *47* (44), 15882–15887. https://doi.org/10.1039/C8DT03202E.
(41) Özcan, M.; Hämmerle, C. Titanium as a Reconstruction and Implant Material in Dentistry: Advantages and Pitfalls. *Materials* **2012**, *5* (9), 1528–1545. https://doi.org/10.3390/ma5091528.
(42) Wang, K.; Yin, Y.; Li, C.; Geng, Z.; Wang, Z. Facile Synthesis of Zinc(II)-Carboxylate Coordination Polymer Particles and Their Luminescent, Biocompatible and Antibacterial Properties. *CrystEngComm* **2011**, *13* (20), 6231–6236. https://doi.org/10.1039/C1CE05705G.
(43) Wang, J.; Wang, Y.; Zhang, Y.; Uliana, A.; Zhu, J.; Liu, J.; Van der Bruggen, B. Zeolitic Imidazolate Framework/Graphene Oxide Hybrid Nanosheets Functionalized Thin Film Nanocomposite Membrane for Enhanced Antimicrobial Performance. *ACS Appl. Mater. Interfaces* **2016**, *8* (38), 25508–25519. https://doi.org/10.1021/acsami.6b06992.
(44) Zhang, Y.; Chang, C.-H. Metal–Organic Framework Thin Films: Fabrication, Modification, and Patterning. *Processes* **2020**, *8* (3), 377. https://doi.org/10.3390/pr8030377.
(45) Gross, E. L.; Leys, E. J.; Gasparovich, S. R.; Firestone, N. D.; Schwartzbaum, J. A.; Janies, D. A.; Asnani, K.; Griffen, A. L. Bacterial 16S Sequence Analysis of Severe Caries in Young Permanent Teeth. *J. Clin. Microbiol.* **2010**, *48* (11), 4121–4128. https://doi.org/10.1128/JCM.01232-10.
(46) Persson, G. R.; Samuelsson, E.; Lindahl, C.; Renvert, S. Mechanical Non-Surgical Treatment of Peri-Implantitis: A Single-Blinded Randomized Longitudinal Clinical Study. II. Microbiological Results. *J. Clin. Periodontol.* **2010**, *37* (6), 563–573. https://doi.org/10.1111/j.1600-051X.2010.01561.x.
(47) Wu, X.-Q.; Ma, J.-G.; Li, H.; Chen, D.-M.; Gu, W.; Yang, G.-M.; Cheng, P. Metal–Organic Framework Biosensor with High Stability and Selectivity in a Bio-Mimic Environment. *Chem. Commun.* **2015**, *51* (44), 9161–9164. https://doi.org/10.1039/C5CC02113H.
(48) Xu, X.; Chen, Y.; Zhang, Y.; Yao, Y.; Ji, P. Highly Stable and Biocompatible Hyaluronic Acid-Rehabilitated Nanoscale MOF-Fe2+ Induced Ferroptosis in Breast Cancer Cells. *J.*

Mater. Chem. B **2020**, *8* (39), 9129–9138. https://doi.org/10.1039/D0TB01616K.
(49) Doonan, C.; Riccò, R.; Liang, K.; Bradshaw, D.; Falcaro, P. Metal–Organic Frameworks at the Biointerface: Synthetic Strategies and Applications. *Acc. Chem. Res. 50* (6), 1423.
(50) Ding, M.; Jiang, H.-L. Improving Water Stability of Metal–Organic Frameworks by a General Surface Hydrophobic Polymerization. *CCS Chem.* **2021**. https://doi.org/10.31635/ccschem.020.202000515.
(51) Brozek, C. K.; Dincă, M. Ti3+-, V2+/3+-, Cr2+/3+-, Mn2+-, and Fe2+-Substituted MOF-5 and Redox Reactivity in Cr- and Fe-MOF-5. *J. Am. Chem. Soc.* **2013**, *135* (34), 12886–12891. https://doi.org/10.1021/ja4064475.
(52) Kang, I. J.; Khan, N. A.; Haque, E.; Jhung, S. H. Chemical and Thermal Stability of Isotypic Metal–Organic Frameworks: Effect of Metal Ions. *Chem. – Eur. J.* **2011**, *17* (23), 6437–6442. https://doi.org/10.1002/chem.201100316.
(53) Han, C.; Zhang, C.; Tymińska, N.; Schmidt, J. R.; Sholl, D. S. Insights into the Stability of Zeolitic Imidazolate Frameworks in Humid Acidic Environments from First-Principles Calculations. *J. Phys. Chem. C* **2018**, *122* (8), 4339–4348. https://doi.org/10.1021/acs.jpcc.7b12058.
(54) Ding, M.; Cai, X.; Jiang, H.-L. Improving MOF Stability: Approaches and Applications. *Chem. Sci.* **2019**, *10* (44), 10209–10230. https://doi.org/10.1039/C9SC03916C.
(55) Scrivens, G.; Ticehurst, M.; Swanson, J. T. Chapter 7 - Strategies for Improving the Reliability of Accelerated Predictive Stability (APS) Studies. In *Accelerated Predictive Stability*; Qiu, F., Scrivens, G., Eds.; Academic Press: Boston, 2018; pp 175–206. https://doi.org/10.1016/B978-0-12-802786-8.00007-3.
(56) Infrared Spectroscopy https://chem.libretexts.org/Bookshelves/Physical_and_Theoretical_Chemistry_Textbook_Maps/Supplemental_Modules_(Physical_and_Theoretical_Chemistry)/Spectroscopy/Vibrational_Spectroscopy/Infrared_Spectroscopy (accessed 2021 -04 -25).
(57) Thermogravimetric Analysis - an overview | ScienceDirect Topics https://www.sciencedirect.com/topics/materials-science/thermogravimetric-analysis (accessed 2021 -04 -25).
(58) Bhatia, A.; Chopra, S.; Nagpal, K.; Deb, P. K.; Tekade, M.; Tekade, R. K. Chapter 2 - Polymorphism and Its Implications in Pharmaceutical Product Development. In *Dosage Form Design Parameters*; Tekade, R. K., Ed.; Advances in Pharmaceutical Product Development and Research; Academic Press, 2018; pp 31–65. https://doi.org/10.1016/B978-0-12-814421-3.00002-6.
(59) Pyridine anhydrous, 99.8 110-86-1 http://www.sigmaaldrich.com/ (accessed 2022 -04 -03).
(60) N,N-Dimethylformamide anhydrous, 99.8 68-12-2 http://www.sigmaaldrich.com/ (accessed 2022 -04 -03).
(61) Hudzicki, J. Kirby-Bauer Disk Diffusion Susceptibility Test Protocol. *undefined* **2009**.
(62) Sulfapyridine melting point standard Pharmaceutical Secondary Standard; Certified Reference Material 144-83-2 http://www.sigmaaldrich.com/ (accessed 2022 -04 -05).
(63) PubChem. Sulfapyridine https://pubchem.ncbi.nlm.nih.gov/compound/5336 (accessed 2022 -04 -05).
(64) Brozek, C. K.; Michaelis, V. K.; Ong, T.-C.; Bellarosa, L.; López, N.; Griffin, R. G.; Dincă, M. Dynamic DMF Binding in MOF-5 Enables the Formation of Metastable Cobalt-Substituted MOF-5 Analogues. *ACS Cent. Sci.* **2015**, *1* (5), 252–260. https://doi.org/10.1021/acscentsci.5b00247.
(65) Moulton, B.; Zaworotko, M. J. From Molecules to Crystal Engineering: Supramolecular Isomerism and Polymorphism in Network Solids. *Chem. Rev.* **2001**, *101* (6), 1629–1658. https://doi.org/10.1021/cr9900432.
(66) HardyDisks - Disk Diffusion Susceptibility Test Procedure - Kirby Bauer. **2011**. https://www.keyscientific.com/files/Other%20Manufacturers/Hardy%20Diagnostics/AST%20Discs/Hardy%20AST%20Disc%20Insert.pdf.

(67) Mirabilio, A. Disc_interpretative_table. *E Coli* 13.
(68) Silva, F.; Lourenço, O.; Queiroz, J. A.; Domingues, F. C. Bacteriostatic versus Bactericidal Activity of Ciprofloxacin in Escherichia Coli Assessed by Flow Cytometry Using a Novel Far-Red Dye. *J. Antibiot. (Tokyo)* **2011**, *64* (4), 321–325. https://doi.org/10.1038/ja.2011.5.
(69) Parvekar, P.; Palaskar, J.; Metgud, S.; Maria, R.; Dutta, S. The Minimum Inhibitory Concentration (MIC) and Minimum Bactericidal Concentration (MBC) of Silver Nanoparticles against Staphylococcus Aureus. *Biomater. Investig. Dent.* *7* (1), 105–109. https://doi.org/10.1080/26415275.2020.1796674.
(70) Nordin, M.-A.-F.; Wan Harun, W. H. A.; Abdul Razak, F. Antifungal Susceptibility and Growth Inhibitory Response of Oral Candida Species to Brucea Javanica Linn. Extract. *BMC Complement. Altern. Med.* **2013**, *13* (1), 342. https://doi.org/10.1186/1472-6882-13-342.

F. Facilities and Cyberinfrastructure

FSC Resources and Capabilities:

Florida Southern College's Polk Science Research Laboratories were used as research facilities.

Powder X-ray diffraction data was collected on a Bruker D_2 Phaser CCD diffractometer.

Single crystal data was collected on a Bruker AXS diffractometer.

Infrared Spectrometry was collected on a Thermo Scientific Nicolet iS5.

Muller Hinton Agar Petri Dishes were used for Kirby-Bauer testing.

Hardy Diagnostics Wickerham card and McFarland latex 0.5 were used for dilutions.

Other College/Facility:

Single crystal data provided by Dr. Greg McManus at Florida Gulf Coast University.

Prior research obtained single-crystal data from the Chemistry, Biochemistry, and Physics (CBP) department of the University of Florida and the University of South Florida.

Dr. Langford in the biology department of Florida Southern College will be providing guidance on future research.

Cyberinfrastructure:

Calculated PXRD values were produced using Accelrys Materials Studio Modeling 4.0 software.